Eberhard Karls University Tübingen
Institute for Astronomy and Astrophysics
High Energy Astrophysics

Development of a Detector Simulator for the eXTP Wide Field Monitor

Thesis submitted for the degree of
Master of Science (M.Sc) in Physics
by
Stephanie Jasmin Klein

Supervisor: Prof. Dott. Andrea Santangelo
Submitted: 14.11.2018

Eidesstattliche Erklärung

Hiermit versichere ich, Stephanie Klein, Matrikelnummer: 4100197, dass ich gemäß des allgemeinen Teils der Studien- und Prüfungsordnung der Universität Tübingen für den Studiengang Physik mit akademischer Abschlussprüfung Master of Science (M.Sc.) vom 30.07.2013 diese Masterarbeit mit dem Titel *Development of a Detector Simulator for the eXTP Wide Field Monitor* selbstständig verfasst und keine anderen als die angegebenen Hilfsmittel und Quellen benutzt habe. Ich versichere, alle wörtlich oder sinngemäß aus anderen Werken übernommenen Aussagen als solche kenntlich gemacht zu haben. Die Arbeit ist weder vollständig noch in wesentlichen Teilen Gegenstand eines anderen Prüfungsverfahrens gewesen und wurde weder vollständig noch in wesentlichen Teilen bereits veröffentlicht.

Tübingen, den 14.11.2018

Stephanie Klein

Zusammenfassung

Ab dem Jahr 2025 wird ein neuer Satellit, die *enhanced X-ray Timing and Polarimetry* (eXTP) Mission, den Röntgenhimmel beobachten. Diese Mission ist ein Zusammenschluss der chinesischen XTP und der europäischen LOFT Missionen und besteht aus vier wissenschaftlichen Instrumenten: dem Wide Field Monitor, dem Large Area Detector, dem Spectroscopic Focusing Array und dem Polarimetry Focusing Array. Mit diesen Instrumenten können polarimetrische, spektroskopische und zeitlich aufgelöste Beobachtungen gleichzeitg durchgeführt und dazu benutzt werden, um das Verhalten von Materie in extremen Bedingungen zu erforschen. Hierzu wird eXTP isolierte und binäre Neutronensterne, Systeme mit magnetischen Feldern bis zu 10^{14}-10^{15} Gauss, und schwarze Löcher beobachten. Das Ziel ist es, starke Wechselwirkungen durch das Finden der Zustandsgleichung von Materie in supernuklearen Dichten zu verstehen, QED Effekte wie Vakuumpolarisation und den Einfluss von starken magnetischen Feldern auf die Lichtausbreitung zu erforschen, und durch die Analyse von Massenakkretierung in stark gravitativen Feldern mehr über die zentralen Objekte zu lernen.

Das Institut für Astronomie und Astrophysik in Tübingen (IAAT) ist Teil des internationalen eXTP Konsortiums, welches sich nicht nur aus großen Instituten der Chinesischen Akademie der Wissenschaften und Universitäten in China, sondern auch aus großen Institutionen in mehreren europäischen Ländern und den USA zusammensetzt. Neben einer wichtigen Führungsrolle im Konsortium und der aktiven Teilnahme in wissenschaftlichen Arbeitsgruppen trägt das IAAT durch die Entwicklung von elektronischen Komponenten für den Large Area Detector und den Wide Field Monitor zum Gelingen der Mission bei. Im Zuge dieser Masterarbeit wurden die Hard- und Softwarekomponenten eines Detektorsimulators, welcher die Eigenschaften und die Funktionsweise der im Wide Field Monitor verwendeten Siliziumdriftdetektoren imitiert, entwickelt und getestet. Dieser Detektorsimulator kann in Zukunft für das Testen der Ausleseelektronik, welche ein Tübinger Beitrag zum Wide Field Monitor sein wird, verwendet werden.

Abstract

In 2025, the *enhanced X-ray Timing and Polarimetry* (eXTP) mission will be launched into a low-earth orbit from the Wengchang Satellite Launch Center in China. The mission, which is a merger of the Chinese XTP and the European LOFT missions, carries four scientific instruments – the Wide Field Monitor, the Large Area Detector, the Spectroscopic Focusing Array and the Polarimetry Focusing Array – which will conduct simultaneous studies in timing, spectroscopy and polarimetry. These instruments will be utilized to study states of matter under extreme conditions, such as ten times the density found in atomic nuclei, warped spacetimes found close to the event horizon of black holes, and magnetic fields of 10^{14}-10^{15} Gauss. To conduct these studies, eXTP will observe isolated and binary neutron stars, systems with strong magnetic fields, especially magnetars, and black holes. The observations are analyzed to find the equation of state of matter at supra-nuclear densities needed to understand the nature of strong interactions, to study QED effects in highly magnetic systems in order to test vacuum polarization and the effect of strong magnetic fields on light propagation, and to observe accretion in the strong-field regime of gravity which will give information about the objects creating these fields.

The Institute of Astronomy and Astrophysics in Tübingen (IAAT) is part of the international eXTP consortium that consists of major institutions of the Chinese Academy of Sciences and Universities in China, in addition to major institutions in several European countries and the United States. Next to an important leadership role in the consortium and the active participation in science working groups for the mission, the IAAT will contribute electronics components for the Large Area Detector and the Wide Field Monitor. Within this work, the hard- and software components of a detector simulator for the Wide Field Monitor's Silicon Drift Detector were developed and tested. This simulator can be used in order to check the performance and functionality of the read-out electronics that will be contributed to the eXTP mission's Wide Field Monitor by the IAAT.

Contents

1 Introduction

With the identification of the Sun as the first observed cosmic X-ray source in 1949, a new field in observational astronomy was born: X-ray astronomy. Within this field it soon became evident that polarization measurements add a new and unexplored dimension to the parameter space when observing cosmic X-ray sources (Weisskopf, 2018). According to Soffitta et al. (2013), X-ray polarization can be used to investigate acceleration processes, for example the ones typical of magnetic reconnection in solar flares, and emission in neutron stars' and white dwarfs' strong magnetic fields. The scattering in asymmetric structures like accretion disks and columns, as well as in ionization cones and molecular tori, can be detected, and fundamental physics in conditions that cannot be created in laboratories, such as very strong magnetic fields and the high regimes of gravity, can be probed. With the help of X-ray polarization, models describing fundamental interactions, for example quantum gravity and the extension of the Standard Model, can be tested.

Electromagnetic waves consist of electric and magnetic fields that are oriented transverse to the direction of the wave motion (Figure 1.1) and are the solutions of the wave equation obtained from Maxwell's equations. Since polarization describes the configuration of these fields, the polarization of an electromagnetic wave can be defined as the direction in which the electric field oscillates (Kaaret, 2014). Often, sources emit random mixtures of waves with different polarizations and no preferred oscillation direction, and are therefore classified as unpolarized. However, when a significant fraction of the emitted waves oscillates in a certain orientation, the source is polarized with a particular polarization degree and a polarization angle. These observables describe the relative amount of polarized photons to all observed photons, and the orientation of the electric field of the electromagnetic wave, respectively (Maier et al., 2014).

According to Kaaret (2014), an electromagnetic plane wave propagating in z-direction with angular frequency ω can be described by a sinusoidally varying electric field of the form

$$\vec{E} = \hat{x}E_x + \hat{y}E_y = \hat{x}E_{0x} \cdot \cos(kz - \omega t) + \hat{y}E_{0y} \cdot \cos(kz - \omega t + \xi) \quad , \tag{1.1}$$

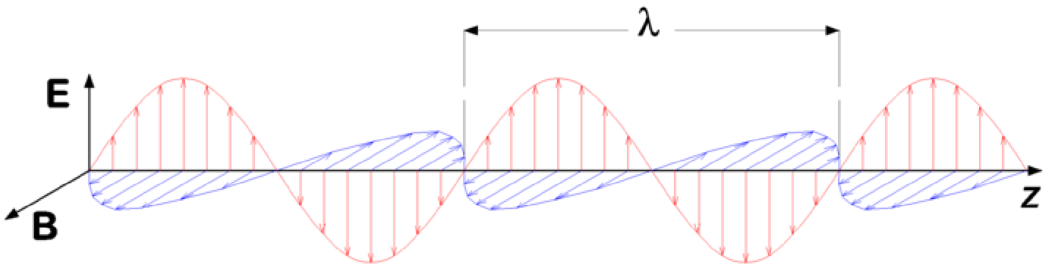

Figure 1.1: An electromagnetic wave of wavelength λ with its electric field vector E (red) oscillating in the vertical direction. The magnetic field B (blue) is always orthogonal to it, and both are perpendicular to the direction of propagation, shown in z-direction. The polarization of an electromagnetic wave is the direction in which the electric field oscillates. Source: Wikipedia contributors (2018).

where E_{0x} and E_{0y} are the amplitudes of the electric field in x- and y-direction, respectively, $k = \frac{\omega}{c}$ is the wavenumber, c is the speed of light, t is the time of propagation, and ξ is the initial phase angle. The polarization angle of the wave is given by the ratio $\frac{E_{0x}}{E_{0y}}$, while the type of polarization depends on ξ: the wave is linearly polarized if $\xi = n\pi$, where n is an integer, while for the case of $\xi \neq n\pi$ the electric field rotates as a function of time (or position) and the polarization is elliptical. Using Stokes parameters (McMaster, 1954), the polarization of a source can be fully characterized:

$$I = \langle E_{0x}^2 \rangle + \langle E_{0y}^2 \rangle \tag{1.2}$$
$$Q = \langle E_{0x}^2 \rangle - \langle E_{0y}^2 \rangle \tag{1.3}$$
$$U = \langle 2 \cdot E_{0x} \cdot E_{0y} \cdot \cos(\xi) \rangle \tag{1.4}$$
$$V = \langle 2 \cdot E_{0x} \cdot E_{0y} \cdot \sin(\xi) \rangle \quad . \tag{1.5}$$

The Stokes parameter V describes the case of elliptical polarization. With these parameters, for which the averages are taken over the photons detected from the source, the polarization degree P and the polarization angle ϕ_0 become

$$P = \frac{\sqrt{Q^2 + U^2 + V^2}}{I} \qquad \text{and} \tag{1.6}$$

$$\tan(2\phi_0) = \frac{U}{Q} \quad , \tag{1.7}$$

respectively. The degree of polarization and the polarization angle depend on the conditions under which the electromagnetic waves are produced. Therefore, by observing these key parameters and by modeling the physical processes such that they are consistent with the observations, the mechanisms that lead to the observed radiation can be investigated (Weisskopf, 2018).

In cosmic X-rays, the only single source of which polarization has been observed so far is the Crab Nebula (see Wolff et al. (1970) and Novick et al. (1971) for examples). For other sources, only upper limits for the degree of polarization are known. With the *enhanced X-ray Timing and Polarimetry* (eXTP) mission, the goal is to improve the sensitivity of X-ray polarization measurements to find polarization degrees and angles for a large number of sources. However, eXTP is not only designed to perform X-ray polarization measurements, but will conduct spectral, timing and polarimetry studies in the energy range of 0.5-30 keV with its four scientific instruments shown in Figure 1.2. The Large Area Detector (LAD) used for spectral timing studies in the energy range of 2-30 keV, has a total area of 3.4 m^2 at 8 keV and, in the current configuration, consists of two panels at the side of the telescope tube (Feroci et al., 2018). The Wide Field Monitor (WFM) located on top of the telescope tube consists of three pairs of coded mask cameras and observes single photon events in the energy range of 2-30 keV to detect sources that will then be studied with follow-up observations by the LAD and the detectors of other observatories (Hernanz et al., 2018). The Spectroscopic Focusing Array (SFA) uses nine of the 13 Wolter I telescopes onbord the mission to conduct spectral timing observations in the energy range of 0.5-10 keV, while the remaining four Wolter I telescopes are used by the Polarimetry Focusing Array (PFA) for spatial, energy and time resolved X-ray imaging polarimetry in the energy range of 2-8 keV (Zhang et al., 2018). By observing isolated and binary neutron stars, systems with strong magnetic fields and black holes, the eXTP mission will study states of matter under extreme conditions. Details about the mission's science case and the instruments can be found in **Chapter 2**.

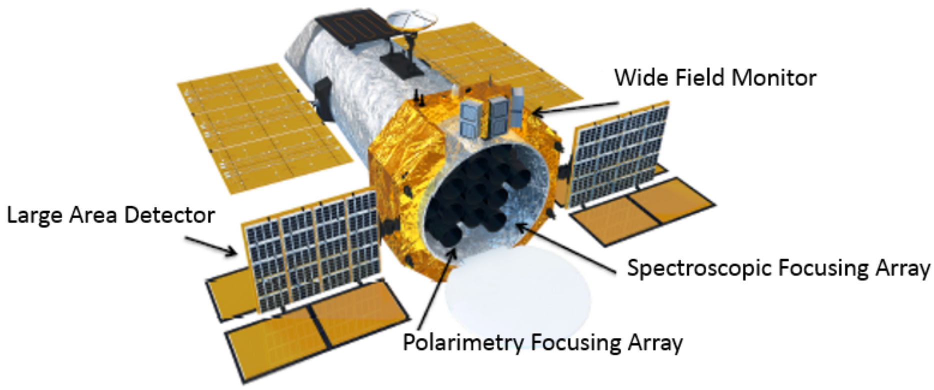

Figure 1.2: The instruments onboard the eXTP mission. Source: Zhang et al. (2018).

The PFA uses a Gas Pixel Detector in order to find the polarization degree and angle for the incoming photons. The other three instruments however use Silicon Drift Detectors (SDDs) to find the energy, arrival time and, in case of the WFM, the incident interaction position of the incoming photons. They use the fact that a photon interaction with silicon produces an electron cloud that, by applying a drift field to the detector, drifts towards anodes, where the charges can be analyzed and used to find information about the incident photon. This process and the SDDs used in the instruments are described in more detail in **Chapter 3**.

The read-out and analysis of the anode charges in the SDDs is performed by dedicated read-out electronics. They will use the data and apply a fit in order to find the initial photon energy, the interaction time and the incident interaction position on the detector. The Institute of Astronomy and Astrophysics in Tübingen (IAAT), which is part of the international eXTP consortium, will contribute the read-out electronics for the LAD and the WFM. The aim of this thesis was the development of a detector simulator for the WFM's SDD in order to test the perfomance and functionality of these electronics.

The detector simulator consists of a software- and a hardware component. The software component on a PC is responsible for the simulation of photons with different energies in different locations on the detector. It calculates the electron distribution on the anodes for each individual photon event and sends this information to the hardware component, which consists of an Field Programmable Gate Array (FPGA, see Section 4.2.1), and saves this information into an onboard memory. When the hardware component receives a "send data" command, it will transmit the saved information for individual photon events to the connected electronics. In addition to the photon event simulation, the software component of the simulator has a feature that reconstructs the initial interaction position and photon energy from the data saved in the memory of the FPGA, and can visualize the interaction positions on the detector based on the reconstructed data. The data transmission between the hardware component and the connected electronics as well as the features of the software component are used to check whether the read-out electronics receive data correctly and reconstruct the correct incident photon energy and interaction positions, or if improvements are needed before the mission is sent into orbit.

The current version of the detector simulator and its components are presented in **Chapter 4**. The final **Chapter 5** concludes this thesis by reviewing the detector simulator developed in the course of this work and by discussing possible improvements and future versions of the simulator.

2 The eXTP Mission

In 2025, a satellite with four scientific instruments will be launched into orbit: the *enhanced X-ray Timing and Polarimetry* (eXTP) mission. With its 13 X-ray grazing–incidence Wolter I telescopes (see Section 2.3.3) in addition to a Large Area Detector and a Wide Field Monitor it will study states of matter under extreme conditions that cannot be created in laboratories, such as densities as high as ten times the one found in atomic nuclei, warped spacetimes found close to the event horizon of black holes, and magnetic fields of 10^{14}-10^{15} Gauss. The current design of the satellite can be seen in Figure 2.1.

(a) Artistic view of the current eXTP design.

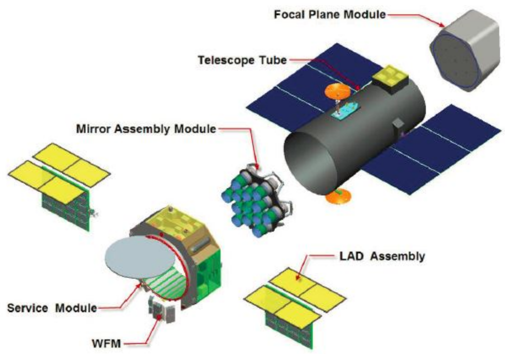

(b) Exploded view of the deployed eXTP satellite with its modules.

Figure 2.1: The current eXTP design. 2.1a shows an artistic view of what the assembled mission might look like, while 2.1b shows an exploded view, depicting the different modules. Source: Zhang et al. (2018).

In the following sections, the mission will be described in more detail: first, the mission profile will be presented, followed by a discussion of the mission's scienctific goals. This chapter is completed by an in-depth description of the instruments onboard of eXTP.

2.1 The eXTP Mission Profile

The eXTP mission is a merger of the Chinese XTP (Dong, 2014) and European LOFT (Feroci et al., 2012) missions. The mission will be launched into an equatorial low-Earth orbit with an inclination of less than 2.5° and an altitude of 550 km. This orbit has been chosen for the robust shielding from solar particle events and cosmic rays by the geomagnetic field as well as the reduction of the time spent in the South Atlantic Anomaly[1] and its effects on the instruments. The eXTP satellite will be launched into orbit from the Wenchang Satellite Launch Center located in Wenchang, Hainan, China, onboard a Long March 7 rocket (Zhang et al., 2018).

The goal of the mission design is to stay within the launch vehicle's maximum carrying capacity, which is 6000 kg, while realizing a maximal focal length and effective detection area, which is important in order to measure and observe weaker fluxes and sources. As can be seen in Figure 2.1b, the mission is composed of four different functional modules:

1. The Mirror Assembly Module, which holds the 13 mirror modules and star trackers of both the SFA and the PFA.
2. The Focal Plane Module, which consists of the 13 focal plane cameras and a sun shield to protect the detectors.
3. The LAD Assembly, which will, after launch, deploy two wings covered with SDDs that have the same pointing direction as the Mirror Assembly Module.
4. The WFM, which consists of six coded mask cameras that simultaneously look at a large fraction of the sky.

Both the Mirror Assembly Module and the Focal Plane Module are supported by the telescope tube, the spacecraft's main structure that helps to achieve the focal length of 5.25 m.

2.2 The eXTP Science Case

The eXTP mission has two operating modes: the pointed observation, which is the main working mode where the principal axis points towards the observed target, and the scan

[1] The South Atlantic Anomaly is a dip in Earth's magnetic field that reaches down to an altitude of about 200 km above the surface, which leads to an increased flux in charged particles and cosmic rays that can damage detectors. The dip is created because the intersection of Earth's rotational axis and its magnetic axis is not at the same location as Earth's midpoint (Snowden, S. L., 2002).

mode, in which the area close to a known source is scanned in order to calibrate the pointing or verify the point spread function[2]. The scan mode is not foreseen to be used for scientific purposes but for calibration only. By simultaneously conducting studies in timing, spectroscopy and polarimetry, these modes are used to fulfill the mission's primary goals, which are included in the mission statement to study the state of matter under extreme conditions, stated below:

1. Finding the equation of state of matter at supra-nuclear density.

2. Studying QED[3] effects in highly magnetic stars.

3. Analyzing accretion in the strong-field regime of gravity.

eXTP will complete these goals by observing bright sources in the Milky Way, such as black holes, isolated and binary neutron stars, and systems with strong magnetic fields, especially magnetars. The mission will also make use of its wide field monitoring capabilities to detect electromagnetic counterparts of gravitational wave sources (Zhang et al., 2018).Unless marked differently, the information of the following subsections is based on Zhang et al. (2016).

2.2.1 The Study of Matter in Ultra-Dense Conditions

Modern physics wants to understand the nature of strong interactions, which is responsible for the state of nuclear matter. In order to achieve this understanding, neutron stars are suitable objects to observe because their physics is also determined by strong interactions. Their matter is compressed by gravity to densities of approximately ten times the one found in atomic nuclei, producing exotic states and phases of matter that relate to extreme temperatures and pressures, such as nuclear superfluids[4], the color

[2]The point spread function, PSF, describes the normalized intensity distribution of the point source image, which means that it describes how an ideal, pointlike object is imaged by the system. For a circular aperture, the theoretically best achievable PSF relation is $I(r) = (\frac{2J_1(\pi r)}{\pi r})^2$, where $J_1(\pi r)$ is the Bessel function of first kind. This gives the best achievable point-image resolution set by diffraction, also known as full width at half maximum (FWHM), which can be calculated by FWHM $\approx \frac{\lambda}{D}$, where λ is the observed wavelength and D is the aperture diameter (Sacek,V., 2015).

[3]Quantum Electrodynamics, the study of the interaction of electromagnetic radiation with electrically charged matter under the account of relativity and quantum mechanics.

[4]At high densities and low temperatures, nucleons inside a neutron star form Cooper pairs due to the long-range attractive nuclear force. This results in a fluid with zero viscosity that does not lose kinetic energy when flowing: a nuclear superfluid (Lombardo and Schulze, 2001).

superconductor phase[5] and strange matter[6] like hyperons[7] and deconfined quarks[8]. Therefore, neutron stars provide access to a parameter space at high densities that is unique, for example high baryon chemical potentials. As shown in Figure 2.2, these high densities in combination with their low temperatures make the observations of neutron stars a complement to the research conducted at the Large Hadron Collider at CERN and other heavy ion collision experiments where high temperatures and low densities are studied. The pressure and density of a neutron star is related by its equation of state, which can be used to intertwine strong interaction physics and observables, and is encoded into the mass vs. radius diagram via stellar structure equations. Using the relation between mass and radius, not only can the equation of state be found, but the microphysics in the neutron star's interior, where extreme densities exist, can be studied. Different equations of state and their corresponding mass vs. radius diagrams are shown in Figure 2.3.

In order to complete the observational goal to measure the mass and radius within a few percent precision for several sources, the eXTP mission will use pulse profile modeling and spin measurements. Figure 2.4 shows the graphic of a neutron star's surface hotspot and a schematic of a pulse profile. The pulse profiles are created by the emission from surface hotspots that develop on fast spinning neutron stars with weak magnetic fields (Watts et al., 2016). Their pulsation amplitude is affected by relativistic effects depending on the neutron star's mass-over-radius ratio, which means, by fitting high quality profiles, the mass and radius can be found. eXTP's polarimetry capabilities will help to constrain both the observer and hotspot inclination angles by making phase-resolved measurements of the polarization degree and angle that are found in the hotspot radiation modulated with the spin phase. Knowing these inclination angles will reduce degeneracies, which in return will help make more precise mass and radius measurements. The key targets for pulse profile observation and modeling are burst oscillation sources and accretion powered millisecond pulsars, which will be observed

[5] In the color superconductor phase, which is thought to be a superfluid and an electromagnetic insulator, two different types of quarks are barely able to pair because of a difference in Fermi momenta, which is the result of different masses or different chemical potentials (Alford, 2001). Alford et al. (2008) describes the color superconductor phase as a degenerate liquid of quarks that undergo Cooper pairing near the Fermi surface. Once the Cooper pairs condense, the color gauge symmetry spontaneously breaks.

[6] Strange matter is a liquid form of quark matter and consists of up, down and strange quarks as opposed to nuclear matter, that only consists of up and down quarks in neutrons and protons, or non-strange quark matter that only contains up and down quarks.

[7] Baryons that contain one or more strange quarks, but no charm, bottom or top quark are called hyperons.

[8] Deconfined quarks can move freely over distances that are larger than one femtometer and form the quark-gluon plasma, which is created at extremely high densities.

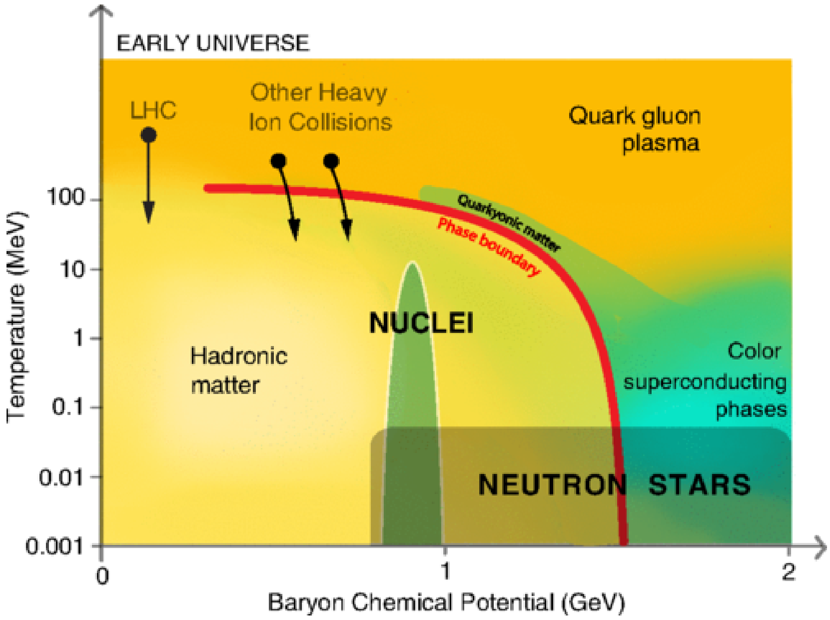

Figure 2.2: Different states of matter that can be studied by observing neutron stars and by conducting laboratory experiments. The baryonic chemical potential stands for the pressure, where 1-2 GeV correspond to approximately 1-6 times the density of atomic nuclei. Quarkyonic matter is a hypothesized phase in which cold dense quarks are confined. Source: Watts et al. (2016).

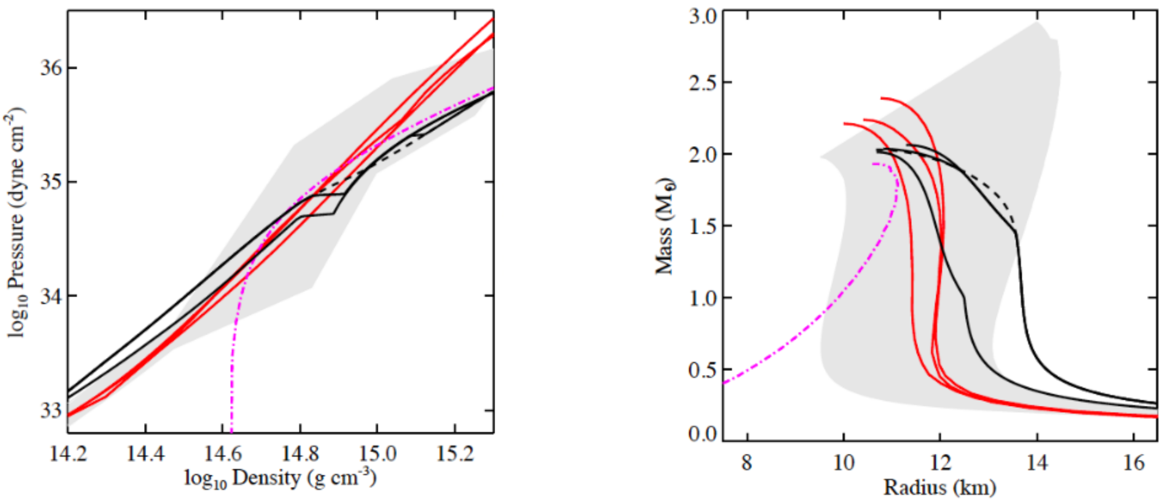

Figure 2.3: Different equations of state and their corresponding mass vs. radius diagrams based on models including different microphysics. Shown are nucleonic equations of state to the highest pressures and masses (red), hybrid models with a strange quark core (solid black curves), hyperon core models (dashed black curves), a self-bound strange quark star model (dash-dotted magenta curve), and a range of parametrized nucleonic equations of state that are based on the chiral effective field theory (for details see Machleidt and Entem (2011)) at low densities (shaded grey bands). Source: Watts et al. (2016).

ranging from a few to several hundred ks.

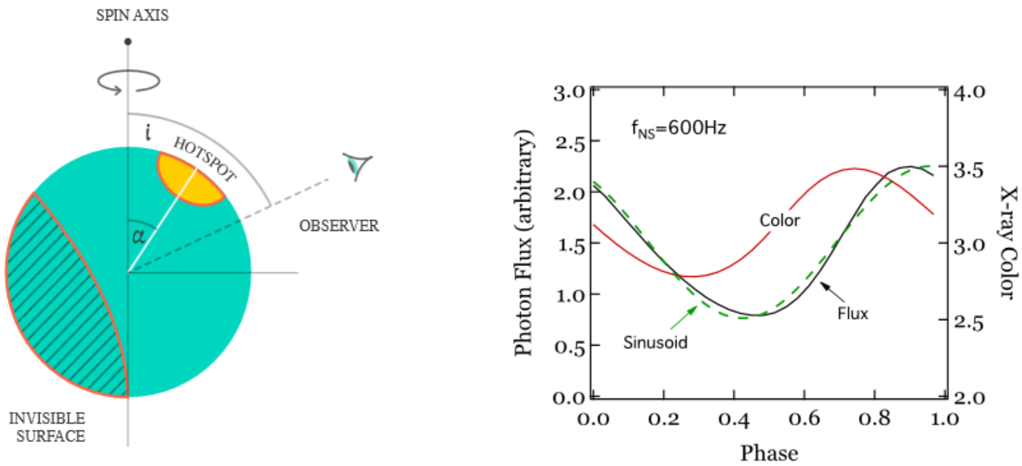

Figure 2.4: *Left*: The graphic of a neutron star's surface hotspot. i describes the observer inclination, while α describes the hotspot inclination. As the neutron star rotates, the emission from the surface hotspot generates a pulsation. Due to relativistic light bending, the invisible surface is smaller than a hemisphere. *Right*: A schematic of the pulse profile and the phase dependence of spectral color for a neutron star spinning at 600 Hz. The waveform is affected by relativistic effects and is modified from a pure sinusoid. Even though the hotspot has a uniform temperature, the spectral color, which is the ratio of the number of photons with energies above to those below the blackbody temperature, is phase dependent. By using the shape of the waveform and the energy dependence, the mass and radius of the neutron star can be found. Source: Watts et al. (2016) and Psaltis et al. (2014), respectively.

The large effective area of eXTP will not only help to constrain the neutron star's equation of state by finding many more neutron star spins, of which the fastest will put more severe constraints on the equation of state, but will also allow a detection of burst oscillations in Type I X-ray bursts[9] to an amplitude of 0.4 %rms[10] in the burst tail and 1.3 %rms in the burst rise. Simulations have shown that pulsation with amplitudes of 0.04 %rms, 0.3 %rms and 1.9 %rms can be found for bright, moderate and faint sources, respectively.

[9]Type I X-ray bursts are thermonuclear flashes on the surface of a neutron star with a weak magnetic field that is part of a binary system with a main sequence star. The flashes happen once the mass that the neutron star accretes from its companion reaches the critical mass. The luminosity profile of a Type I X-ray burst shows a sharp rise time of approximately one second, which is followed by a slow and gradual decline over approximately 60 seconds. The bursts happen in irregular intervals with some sources being inactive for weeks to months, and can range from hours to days. In comparison, a Type II X-ray burst has a quick pulse shape and multiple fast bursts within minutes. So far, only a couple of Type II bursts have been observed (Woodruff, J, 2007).

[10]Root mean square, the square root of the arithmetic mean of the squares of a set of numbers.

2.2.2 The Physics and Astrophysics of Strong Magnetic Fields

A deep understanding of the physics of strong magnetic fields will be provided by targeting magnetars, accreting X-ray pulsars and rotation-powered pulsars with the broadband, high sensitivity, polarimetry and monitoring capabilities of eXTP. Studies of QED effects will also be enabled by the mission.

Magnetars, which are highly variable X-ray sources, have magnetic fields of the order of 10^{14}-10^{15} Gauss and fluxes that can change by order of magnitudes. Their variability extends from short bursts ($< 1\,\mathrm{s}$) over intermediate flares ($\sim 1 - 40\,\mathrm{s}$) and giant flares ($\sim 500\,\mathrm{s}$) to outbursts, which can have a duration of several weeks to years. eXTP is expected to find a new magnetar candidate every year due to their high variability and the WFM's large sky coverage shown in Figure 2.14. This coverage provides the opportunity to observe a large fraction of the Galactic Plane during pointings, enabling the spin period observation and monitoring of several magnetars at the same time, which makes it possible for eXTP to detect glitches[11] and precession, which is the change in the orientation of the rotational axis, as well as to measure braking indices[12].

Another key target is accreting X-ray pulsars, whose emerging radiation and its polarization properties will be important. Depending on the geometry of the emission region, the X-ray linear polarization varies with the energy and the pulse phase, and can reach polarization degrees of up to 70 %. As shown in Figure 2.5a, the exposure time of phase-resolved studies for bright sources is approximately 10 ks, while the one for weak sources is approximately 100 ks in order to constrain the linear polarization fraction to better than 10 %. These long exposure times will produce high quality pulse profiles, and will extend studies on the luminosity dependence of the cyclotron resonance scattering feature[13] while investigating the criteria for accreting pulsars to switch

[11] Glitches are sudden jumps in the frequency Ω of a pulsar of the order $\frac{\Delta\Omega}{\Omega} \approx 10^{-6}$. A possible explanation for them is that the rotational vortices in the neutron superfluid are pinned to the crystal structure of the neutron star's crust. Because of the proportionality of the superfluid's rotation frequency with the density of the vortices, the vortices move outward when the neutron star's spin slows. The stress that is produced by this movement is released in the form of glitches (Alford et al., 2008).

[12] The braking index reveals physical expectations as to why the spin of stars should slow down. It can be calculated by $n \equiv \frac{\Omega\ddot{\Omega}}{\dot{\Omega}^2} = \frac{\nu\ddot{\nu}}{\dot{\nu}^2} = 2 - \frac{P\ddot{P}}{\dot{P}^2}$, where Ω is the angular velocity, $\dot{\Omega} = -K\Omega^n$ is the first derivative of Ω with the proportionality constant K, $\nu = \frac{\Omega}{2\pi}$ is the spin frequency and $P = \frac{1}{\nu}$ is the spin period. As an example, n=1 points towards particle-wind radiation and n= 5 points towards a gravitational wave emission as reasons for a declining spin (Gao et al., 2016).

[13] When the radiation that is emitted by the accretion column is reflected from the neutron star's surface, cyclotron lines, also called cyclotron resonance scattering features, are formed. According to Mushtukov et al. (2014), the neutron star's magnetic field channels the accreting gas towards the magnetic poles, which leads to a line-like absorption feature in the form of cyclotron lines in

from local super-Eddington to sub-Eddington accretion[14]. By analyzing the energy and luminosity dependence of the pulse profiles and cyclotron lines due to the long exposure times (for an example see Figure 2.5b), the relation between the phase dependence of the polarization properties and the geometry of the emission region will be studied. According to Jaisawal and Naik (2016), the line energy and luminosity are positively correlated in low-luminosity sources, while it is negatively correlated or not correlated at all in high-luminosity sources. As described in Klochkov et al. (2012), the different correlations are due to whether a source is undergoing super- or sub-Eddington accretion. In super-Eddington accreting sources, the infalling matter is decelerated in a radiative shock. The height of this shock increases with the luminosity of the source, meaning it drifts to an area with a lower magnetic field strength. In sub-Eddington accreting sources, the infalling matter is slowed down by the Coulomb drag[15] and plasma effects. With increasing luminosity, the height of the emitting region decreases due to an increase in ram pressure of the infalling material, which in return leads to a positive $\frac{\mathrm{E_{cyc}}}{\mathrm{flux}}$ relation. Details about the correlation of line energy and luminosity can be found in Becker et al. (2012).

For one of the first predictions of QED, which are vacuum polarization and the effect of strong magnetic fields on light propagation, the eXTP mission will supply the first tests. By observing neutron stars and magnetars, the existence of the effect can be verified, while the effect for the latter is the strongest due to the magnetars' strong magnetic fields. The linear X-ray polarization is enhanced by vacuum birefrin-

the X-ray spectrum. The absorption features are due to a resonant scattering between the hard X-ray photons and electrons in quantized states, the so called Landau levels, which depend on the strength of the magnetic field and are equally spaced. The energy of the cyclotron resonance scattering corresponds to the separation of the levels and can be calculated by $E_{\mathrm{cyc}} = \frac{11.6B}{1+z}$ keV, where B is the magnetic field in 10^{12} G and z is the gravitational redshift (Jaisawal and Naik, 2016).

[14] The Eddington limit describes the case in which the gravitational force acting on an electron-ion pair in the gas surrounding a star is exactly equal to the radiation pressure that radiates spherically outward. If this limit is exceeded, the gas is blown away. The Eddington limit, also called Eddington luminosity, can be calculated by $L_{\mathrm{edd}} = \frac{4\pi G M m_p c}{\sigma_T}$, where G is the gravitational constant, M is the mass of the central object, m_p is the mass of a proton and σ_T is the Thompson cross section. For pure ionized hydrogen, the Eddington luminosity becomes $L_{\mathrm{edd}} = \frac{4\pi G M c}{\kappa}$, where $\kappa = \frac{\sigma_T}{m_p}$ describes the opacity of stellar material. The mass accretion rate for the Eddington limit is $\dot{M}_{\mathrm{edd}} = \frac{L_{edd}}{\eta c^2}$, with η being the efficiency of the accretion disc. If the mass accretion rate of an object is higher than the Eddington limit mass accretion rate, for example due to non-spherical accretion, the object undergoes Super-Eddington accretion. In the other case, if the mass accretion rate of an object is lower than the Eddington limit mass accretion rate, sub-Eddington accretion takes place (Abramowicz and Straub, 2014).

[15] Coulomb drag is a transport phenomenon whereby long-range Coulomb interaction between charge carriers in two closely spaced but electrically isolated conductors induces a voltage (or, in a closed circuit, a current) in one of the conductors when an electrical current is passed through the other (Narozhny and Levchenko, 2016).

gence[16] from about $5 - 10\,\%$ to nearly $100\,\%$. For neutron stars with a magnetic field of 10^{12} Gauss, this effect is nearly as strong.

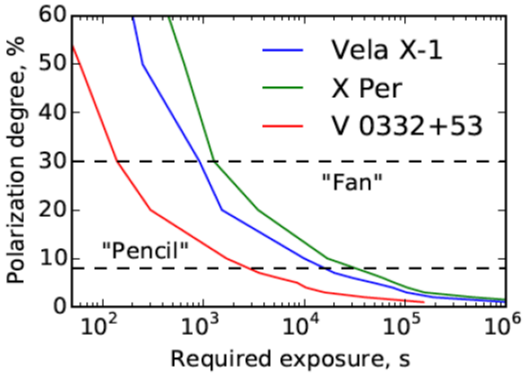

(a) Required exposure time to constrain the linear polarization degree to better than 10 %.

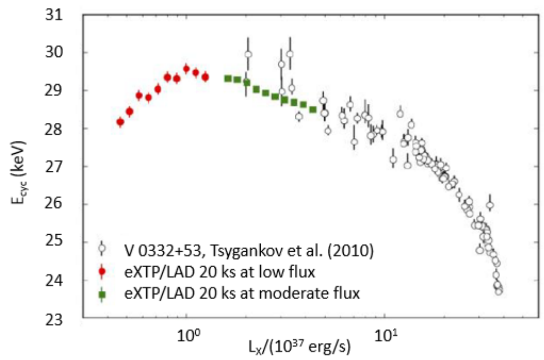

(b) Variation of the cyclotron line energy with luminosity for V0332+53.

Figure 2.5: The required exposure time to constrain the linear polarization degree to better than 10 % for three different cases is shown in 2.5a. Blue: Vela X-1, a bright source ($F_{2-10keV} \sim 1.6 \times 10^{-9}\,\frac{\mathrm{erg}}{\mathrm{s{\cdot}cm^2}}$); Green: X-Per, a weak persistent source ($F_{2-10keV} \sim 6 \times 10^{-10}\,\frac{\mathrm{erg}}{\mathrm{s{\cdot}cm^2}}$); Red: V0332+53, a Be transient in outburst ($F_{2-10keV} \sim 1.6 \times 10^{-8}\,\frac{\mathrm{erg}}{\mathrm{s{\cdot}cm^2}}$). 2.5b shows the variation of the cyclotron line energy with luminosity for V0332+53. The line energy at low luminosities can be measured by the LAD, which will extend the study of the correlation between line energy and luminosity. The red markers are 20 ks observations at low flux, while the green markers are observations of the same length for a moderate flux. Source: Zhang et al. (2016).

2.2.3 The Physics of Accretion in Strong Gravitational Fields

In order to investigate the physics of accretion in strong gravitational fields, the study of matter close to the event horizon of black holes is very suitable. Looking at the motion of matter near super-massive and stellar-mass black holes gives information about the deep potential well that is generated by the central object, its mass and spin, and helps to verify predictions made by general relativity in the strong-field regime. Relativistically broadened Fe lines and relativistic time-scale variability, for example

[16] In vacuum, electromagnetic radiation propagates along two modes: the ordinary mode (O mode), in which the electric field oscillates parallel to the magnetic field plane, and the extraordinary mode (X mode), in which the electric and magnetic field planes are orthogonal to each other. In strong magnetic fields virtual electron/positron pairs are created, leading to a change in the refractive indices proportional to B^2 along the X and O modes. This change in the refractive indices affects the propagation, causing a change in the polarisation degree of the electromagnetic radiation, called birefringence (Mignani et al., 2017).

quasi-periodic oscillations, are used to investigate the behavior of matter in the strong–field regime. The spectral resolution needed to resolve the relativistically broadened Fe lines as well as the large photon throughput required to study their variability to time scales below the dynamic time scale of the strong-field regime are provided by the eXTP mission. Additionally, the accretion and ejection flows around black holes will be studied for the first time with polarization information obtained by eXTP.

As a simulation discussed in Zhang et al. (2016) shows, the eXTP mission can make measurements of the inner disc's radius of a 0.5 Crab[17] black hole with maximal spin (for example GRO J1655-40) and its radial emissivity within $1-2\,\%$ accuracy in the unprecedented short time of 100 s. The black hole's spectrum and the confidence levels for the disc emission vs. the inner radius are shown in Figure 2.6. This short observation time offers the possibility of studying the innermost region and variability on time-scales comparable to different outflow components, for example winds and jets, and will ultimately provide a link on how ejection is linked to the inner accretion flow. The mission's energy resolution in combination with the large effective area and the broadband coverage of both the SFA and the PFA not only enables a disentanglement of the spectral complexities in the Fe-K region[18], but also allows measuring the reflection continuum shape. According to Noda (2015), reflection components are created when the primary continuum is Compton scattered and/or photo-absorbed by neutral/ionized materials that surround the central black hole, for example the accretion disk. Due to this scenario, photons in the high energy band lose their energy due to the Compton down scattering, while in the low energy band the reflection continuum is created by the photo-absorption process. The continuum has a hard spectral shape and is responsible for the Fe-K absorption edge at ~ 7.1 keV. The measurement of the reflection continuum shape leads to the extraction of relativistic reflection parameters and the recovery of the black hole spin to an accuracy of 10 %.

The mission's broadband coverage from $0.5-30$ keV together with the high energy resolution and the large photon throughput make a simultaneous measurement of Fe-K lines, the reverberation lags of the disk blackbody and Compton reflection humps, explained below, possible. According to De Marco and Ponti (2016), accreting black hole systems are emitting X-rays from the inner Comptonizing region. They illuminate the surrounding matter, of which the dense material from the optically thick disk responds

[17]Crab is the measurement of intensity of X-ray sources and describes the intensity of the Crab Nebula at the corresponding X-ray photon energy of the observed object. For photons in the range of 2-10 keV, one Crab corresponds to 15 $\frac{\mathrm{keV}^2}{\mathrm{keVcm}^2\mathrm{s}}$.

[18]Fe-K lines are located at around 7.1 keV (Noda, 2015).

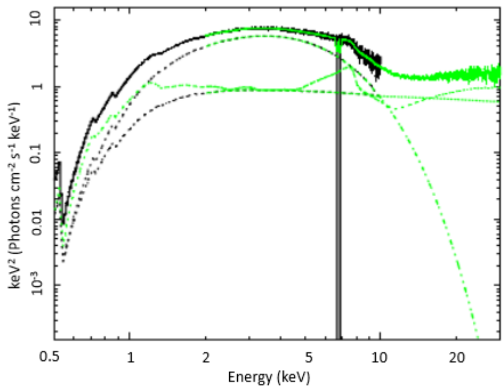

(a) Simulated eXTP spectrum of a 0.5 Crab black hole for an exposure time of 100 s.

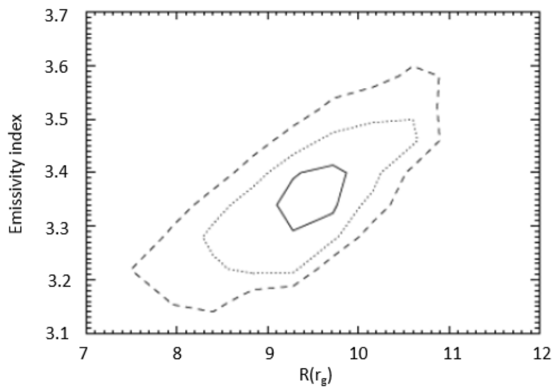

(b) Simulated confidence levels for the disc emission vs. inner radius.

Figure 2.6: The simulated eXTP broadband spectrum of a 0.5 Crab, maximally rotating X-ray burst black hole like GRO J1655-40 for an exposure time of 100 s is shown in 2.6a. The confidence level of disc emission vs. radius for the same source is depicted in 2.6b. The solid, dotted and dashed lines represents confidence levels of one, two and three sigmas, respectively. Source: Zhang et al. (2016).

quasi instantaneously to the X-ray irradiation. The time delay between the primary and the reprocessed emissions is the light crossing time between the two regions and is observed as reverberation lags that are a tracer for the geometry of the innermost accretion flow. As Reynolds (1999) states, the X-ray reflection imprints atomic features onto the observed spectrum because the cold matter in the disk that is close to the X-ray emitting hot matter intercepts and reprocesses a fraction of the primary X-ray continuum. This leads to the Compton reflection humps, which can be observed around 30 keV. Measuring Fe-K lines, the reverberation lags of the disk blackbody and Compton reflection humps give separate information about the inner disk radius, allowing an accurate and independent determination of the black hole spin. Adding the spectral-timing approach, the accuracy of disk thermal fitting is enhanced, which is used to map the innermost regions and to measure the black hole spin.

The high sensitivity of the eXTP instruments will enhance the study of Quasi-Periodic-Oscillations (QPOs). The mission can measure the QPO's waveform either directly or by Fourier reconstruction. The direct approach will for the first time allow a coherent detection, where an adequate number of photons will be collected within the signal's coherence time[19]. So far, this approach has been limited to a few high-coherence low-frequency QPOs. However, the achieved signal-to-noise ratio and spectral resolu-

[19]The coherence time is the time span over which a propagating wave is coherent, meaning that its phase is predictable. The coherence time can be calculated with $\tau = \frac{1}{\Delta v} = \frac{\lambda^2}{c\Delta\lambda}$, where λ is the

tion have not been good enough to study the phase dependence of the spectral shape. With eXTP, the direct approach will be common for low-frequency QPOs and neutron star kHz QPOs. Additionally, the LAD will provide a phase-resolved spectroscopy study of QPOs, leading to a detection of the change in shape of the iron line as a function of the QPO phase.

Combining the data obtained by the LAD and the PFA, eXTP enables the combination of X-ray polarimetric and timing information. This combination is obtained by cross correlating the photon polarization signal of the PFA with the high signal-to-noise light curves of the LAD, making it possible to determine the time dependent polarization signal in a similar manner to spectral-timing measurements like reverberation and QPO phase-resolved studies. This enables the determination of the accretion flow geometry and will put limits on the black hole spin and other key parameters.

2.3 The Instruments

eXTP will fulfill its scientific goals with the help of its instruments, namely the Large Area Detector, the Wide Field Monitor, the Spectroscopic Focusing Array and the Polarimetry Focusing Array. In the following sections each instrument will be introduced. The presented information is mainly based on Zhang et al. (2018), however, for the LAD and the WFM additional sources (Feroci et al. (2018) and Hernanz et al. (2018), respectively) have been used. Details about the SDDs utilized in the instruments will be given in Chapter 3.

2.3.1 The Large Area Detector

With its large collecting area, the LAD, of which the main specifications can be found in Table 2.1, will observe single photon events in an energy range of $2-30\,\mathrm{keV}$. This range will be extended to $30-80\,\mathrm{keV}$ for out of field of view burst events as the collimator becomes transparent. The instrument's large effective area of $\sim 3.4\,\mathrm{m}^2$ at $8\,\mathrm{keV}$ is the reason that eXTP's most important science case, which is to determine neutron stars' radii and masses, and to investigate gravitation in strong magnetic fields, is fulfilled. Spectral timing studies will be made possible by the high resolution measurement of the arrival time and energy of each photon for a large number of events. The LAD's large area SDDs and capillary plate collimators form the X-ray detectors, each with a thickness of a few mm and a weight of a few hundred grams, which in comparison to

central wavelength of the source, Δv is the spectral width in units of frequency and $\Delta\lambda$ is the spectral width in units of wavelengths.

proportional counters and mechanical collimators of the past generation of large area instruments yield a reduction of weight, volume and power requirements by an order of magnitude.

Table 2.1: The main specifications of the Large Area Detector. Source: Feroci et al. (2018).

Parameter	Specification
Energy range	2-30 keV; extended to 30-80 keV for out of field of view events
Effective area	3.4 m^2 at 8 keV; 0.9 m^2 at 2 keV; 0.3 m^2 at 30 keV
Field of View	1° (FWHM)
Absolute time accuracy	<10 µs
Deadtime	<1 % at 1 Crab
Background	<10 mCrab
Maximum flux	>500 mCrab sustained; >15 Crab continuous over 300 min

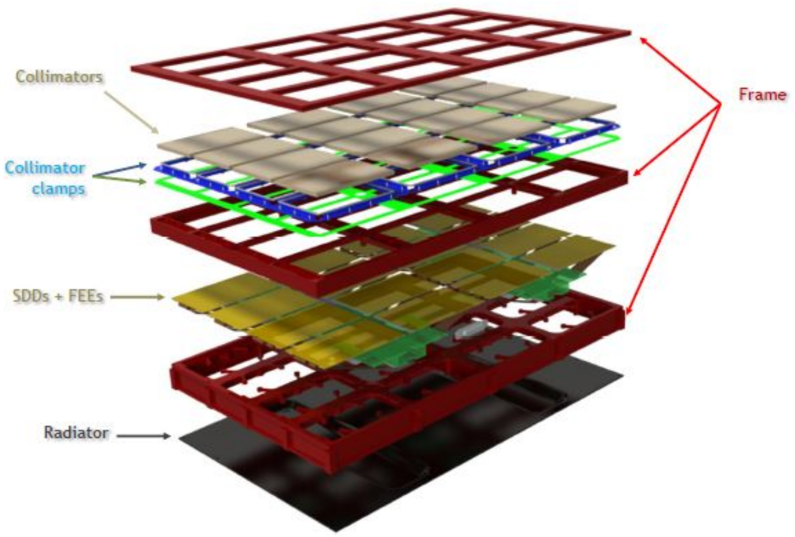

Figure 2.7: Exploded view of the LAD modules' assembly. Each module consists of a 300 µm thick lead back shield (not shown), a 2 mm thick aluminum radiator, a detector and a collimator tray, holding 16 large area SDDs and FEEs, and 16 capillary plate collimators, respectively. Source: Zhang et al. (2018).

The LAD consists of two panels which both hold 20 modules with a 5 × 4 modules configuration. The module assembly can be seen in Figure 2.7. Each module is formed of a 300 µm thick lead back shield to reduce the background events in the SDDs, a 2 mm thick aluminum radiator dissipating heat from the module to the backside of the module box in addition to a detector and a collimator tray, holding 16 large area SDDs and 16 capillary plate collimators, both in a 4×4 configuration, respectively. The capillary plate collimators, shown in Figure 2.8, are a compact design of a mechanical structure with micro-channel plates. They consist of a 5 mm thick sheet of lead glass with the dimensions of the SDD, perforated by thousands of round micro-pores with a diameter of 83 µm. They limit the field of view to 0.98° reducing both source confusion and the X-ray background. The detector tray not only holds 16 SDDs and Front End Electronics (FEE), which amplify and digitize anode charge pulses, but also interfaces the Module Back End Electronics (MBEE), one of two levels of the LAD's Back End Electronics (BEE), the other one being the Panel Back End Electronics (PBEE). The overall panel structure consists of a carbon fiber reinforced plastic, which withstands the launch and brings both mechanical and thermo-elastic stability as well as thermal control to the modules and the PBEE it supports.

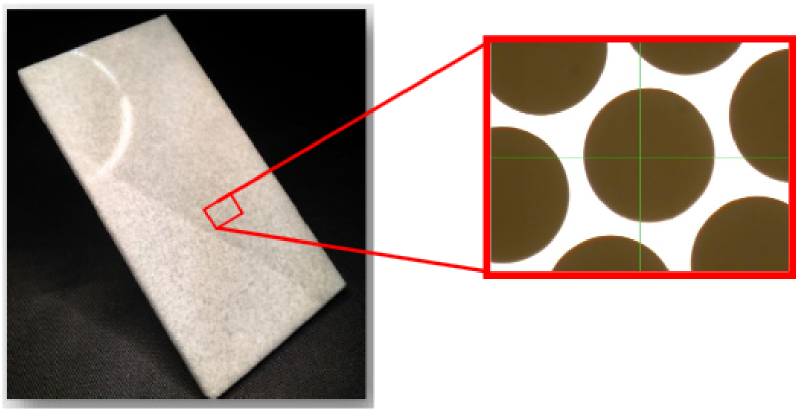

Figure 2.8: The prototype of the LAD capillary plate collimator. This prototype was fabricated by North Night Vision Technology (NNVT, Nanjing, China). The red-framed inlet shows a sketch of the round micro-pores. Source: Feroci et al. (2018).

In order to enable the high-density readout of each detector, 8×32 channel IDeF-X HD Application-Specific Integrated Circuits (ASICs, see Section 4.2.1) with a high performance and low power (17 electron rms with 650 $\frac{\mu\mathrm{W}}{\mathrm{channel}}$, Feroci et al. (2018)) in addition to 1×16 channel OWB-1 ASICs for analog-to-digital conversions are used. The energy resolution for events in the $2 - 30$ keV range is 60 eV, whereas $30 - 50$ keV events, which are used for the study of timing properties of bright sources and hard events outside the field of view, are transmitted with a reduced energy information of 2 keV bins. As can be seen in Figure 2.9, the ASICs are implemented on the rigid-flex printed circuit board (PCB) that not only forms the FEE but also has a flat cable connection to the MBEE, and are directly wire-bonded to the SDD's anode pads.

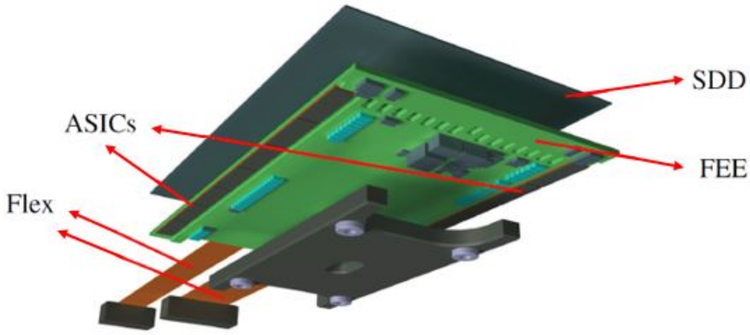

Figure 2.9: Schematic of the LAD Front End Electronics. Source: Zhang et al. (2018).

Once a previously set threshold in one of the ASIC channels is exceeded by the collected signal charge, a trigger is forwarded to the BEE. If the trigger is confirmed, the signals in all ASICs are digitized and sent to the BEE, where, after the analog-to-digital conversion, the processing pipeline is started: each event will be time tagged, the pedestal (the background due to the electronic devices) and common noise will be subtracted, and the event parameters will be determined by reconstructing the energy. The energy reconstruction will be explained in Chapter 3. However, the BEE is not only in charge of event processing, but also of the FEE and the Power Supply Unit. It also creates both housekeeping data and ratemeters, and is responsible for passing formatted event packets along. As mentioned above, the BEE has two hierarchical levels. The MBEE is located at the back of the detector tray and is organized into two PCBs, interfacing eight SDDs each, which it controls along with the FEE and the Power Supply Unit. The MBEE reads out the digitized events of the FEE and is responsible for creating housekeeping data and ratemeters as well as for the formatting and time stamping of events, which will be passed on to the PBEE, the second level of the BEE. Four PBEEs, each interfacing 10 modules, can be found on the panels' back sides. They send commands to the MBEE, distribute clocks and power, and interface all MBEEs with the Instrument Control Unit (ICU) by collecting and buffering the received event packets as well as reorganizing data depending on the observation mode before passing the received science and housekeeping data on to the ICU.

The ICU, which is in cold redundancy, is the central controlling element with access to all instrument subsystems and acts as interface to the spacecraft's onboard data handling system. It consists of three components: the data handling unit, which receives data from the PBEE, the mass memory, and the power distribution unit. The

ICU executes and distributes telecommands, has access to mass memory as well as time distribution and synchronization, processes and compresses data, collects housekeeping data and monitors instrument health.

The LAD is completed by an optical filter on top of the modules (Figure 2.10) consisting of a 1 µm thick substrate in Polyimide of which one side is coated with a 120 nm aluminum layer. The filter enables a light tightness of 10^{-6} transmission in the IR/Visible/UV bands, while more than 90 % will be transmitted at energies larger than 2 keV (Feroci et al., 2018).

Figure 2.10: The LAD optical light blocking filter. This Polyimide filter will enable a light tightness of 10^{-6} transmission in the IR/Visible/UV bands, while more than 90 % will be transmitted at energies larger than 2 keV. Source: Zhang et al. (2018).

2.3.2 The Wide Field Monitor

The WFM consists of three pairs of coded mask cameras that are used to detect sources for follow-up observations with the LAD (Hernanz et al., 2018). The specifications of the WFM can be found in Table 2.2. As Figure 2.11a shows, the central camera pair is observing along the central axis of the satellite, while the other two pairs are tilted by 60°. Each camera pair, in which the cameras are oriented orthogonal to each other (Figure 2.11b), has a field of view of $\sim 90° \times 90°$ at zero response while observing in the 2-50 keV energy range with an energy resolution of $\sim$ 300 eV at 6 keV. For each photon, the energy, incident x- and y- positions on the detector (with an accuracy of <8 mm and <60 µm, respectively) and the time of the event with an accuracy of 1 µs are determined. The cameras, whose design is shown in Figure 2.12, consist of one detector tray each, holding four SDDs, shielded by four 25 µm thick Beryllium windows to protect them against micro meteoroids and debris, four FEEs, one BEE assembly, one collimator and a coded mask with a thermal blanket.

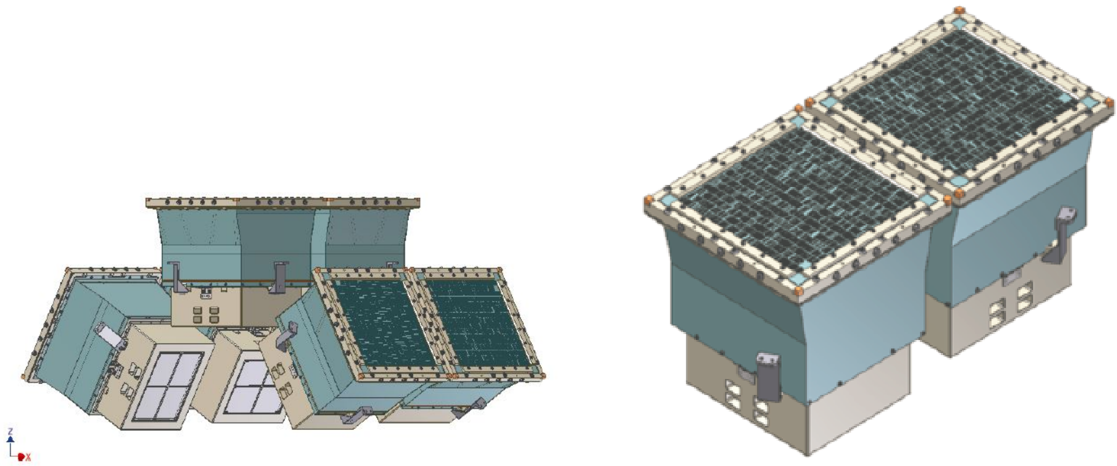

(a) The WFM camera configuration.

(b) One WFM camera pair.

Figure 2.11: The configuration of the WFM cameras is shown in 2.11a. While the central camera pair observes along the central axis, the other two pairs are tilted by 60° from the central axis. As can be seen in 2.11b, the cameras in one camera pair are oriented orthogonal to each other, which enables a source position reconstruction in two coordinates. Source: Zhang et al. (2018) and Hernanz et al. (2018), respectively.

Table 2.2: The main specifications of the Wide Field Monitor. Source: Hernanz et al. (2018).

Parameter	Specification
Energy range	2-50 keV
Effective area	1080 cm^2 for all six cameras
Field of View	5.5 steradian at zero response; camera: $\sim 90° \times 90°$ at zero response
Energy resolution	<300 eV at 6 keV
Time resolution	<300 s for images; <10 µs for event data
Peak sensitivity in LAD direction	0.6 Crab over 1 s; 2.1 mCrab over 50 ks
Burst trigger scale	10 ms-300s
Number of Gamma Ray Burst triggers	> 1 trigger per orbit

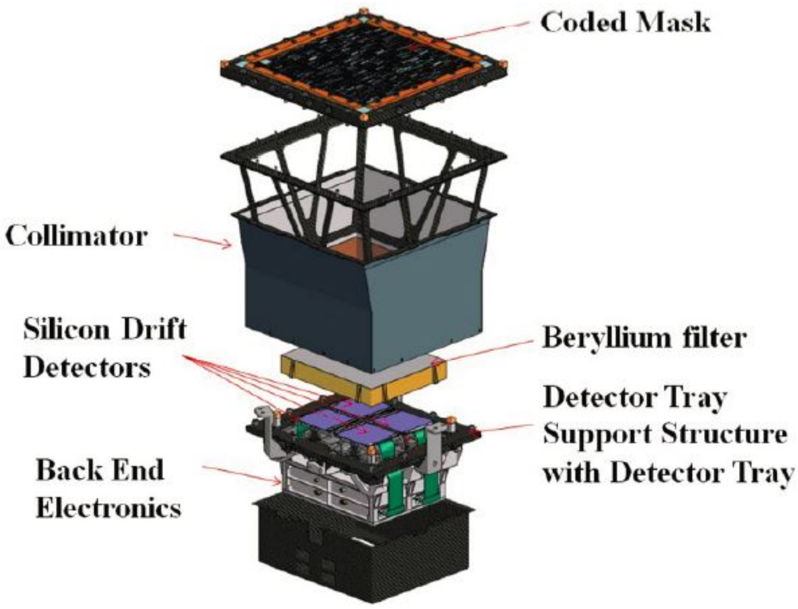

Figure 2.12: Exploded view of the WFM camera design. The coded mask frame is supported by a collimator. The Silicon Drift Detectors are shielded by Beryllium windows. Underneath the SDDs, the Back End Electronics can be found. Source: Zhang et al. (2018).

The coded mask is a 150 µm thick $260 \times 260\ \mathrm{mm}^2$ tungsten foil with strict requirements for flatness and positional stability under thermal fluctuations in order to give accurate source positions. The shadow cast onto the detector due to the mask's pattern is used to reconstruct the direction of the incoming photons. This pattern consists of 1040×16 open and closed elements with a pitch of $250\,\mu\mathrm{m} \times 16.4\,\mathrm{mm}$, leading to an open fraction of $\sim 25\,\%$ which ensures enough flux when observing weaker sources. The chosen detector-mask distance of 202.9 mm assures the required angular resolution of 4.25 arcmin in the fine mask pitch direction and 4.5° in the coarse direction. The angular resolution at full width half maximum for viewing in the on-axis direction can be calculated with

$$\text{resolution} = arctan(\frac{p}{d}) \quad , \tag{2.1}$$

where p is the mask pitch and d is the detector-mask distance. Since the cameras in a camera pair are orthogonal to each other, the combination of the camera images makes the fine position resolution in the two coordinates possible. This is shown in Figure 2.13. The coded mask frame is supported by a collimator made of a light and carbon fiber reinforced polymer, which avoids deformations due to accelerations during launch or thermal stress during operation of the WFM. The collimator is covered by a tungsten sheet to shield background and on its inner part has copper and molybdenum plates used for in-flight energy calibration.

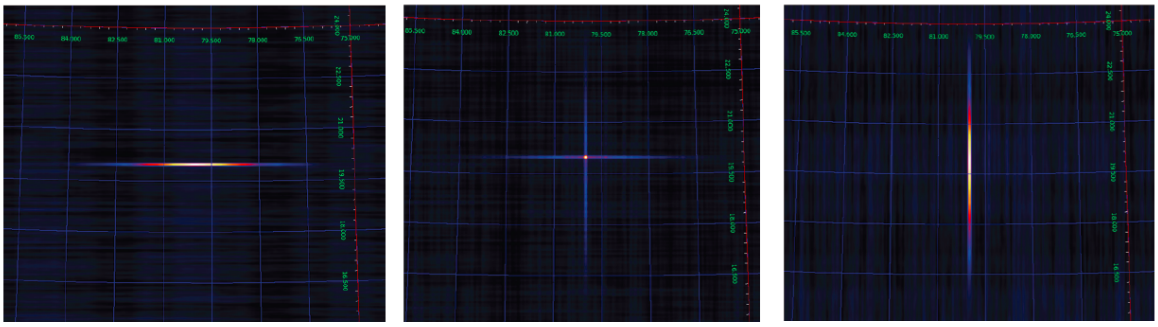

Figure 2.13: Reconstruction of the source position in two dimensions. Due to the position of the two cameras, the reconstruction (middle tile) is made possible by combining the images taken by the camera pair (left and right tiles). Source: Hernanz et al. (2018).

Since the coded mask has to stay flat to ±50 µm over the entire surface for the full operational temperature range of −30 °C to −3 °C, meaning that the temperature gradients between sunlit and dark parts of the orbit cannot exceed 10 °C, the mask is covered by a thermal blanket and the WFM has a sun shield (Hernanz et al., 2018). The collimator is surrounded by a multi-layer insulation blanket offering optimal protection for the SDDs and FEE as well as keeping the camera alignment in the desired margin. The backside of the BEE box will serve as a radiator and transfer the power dissipated by the BEE to the optical bench and the deep sky.

The BEE consist of only one level since only four detectors have to be read out. Each BEE is located at the bottom of the camera and has a similar processing hierarchy as the LAD's BEE described in 2.3.1. Because they analyze the charge distribution over the anodes for each event and with that determine the energy amplitude, anode position and the drift position for each photon, the FPGAs that the BEE is based on have to be larger, faster and more flexible than the ones used in the LAD. In addition to analyzing the event data, the BEE transmits science and housekeeping data to the ICU. The ICU has a main and a redundant unit in separate boxes consisting of the payload data handling unit including a mass memory and a power distribution unit. The ICU controls each camera independently and is able to do real time on-board computations to locate bright transient events.

With the largest field of view of all eXTP instruments, the WFM is expected to detect approximately 100 Gamma-ray bursts (GRB) per year. Although not part of a top level science goal, a burst alert system is implemented. In this system, a network of small ground stations is informed about the time and sky position of the bursts via a very high frequency transmitter within 30 s of the burst in order to ensure a fast follow-up of the GRB afterglow. In addition to the burst alert system, a large number of known high-mass X-ray binaries will be monitored by the WFM, which is a crucial part in finding counterparts for gravitational wave sources. A comparison of the WFM field of view with other sky monitoring X-ray instruments is shown in Figure 2.14.

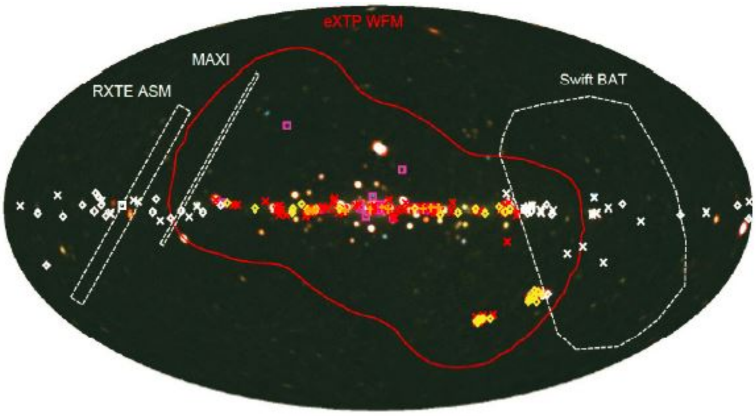

Figure 2.14: A comparison of the WFM field of view with other all sky monitoring instruments. RXTE ASM is the Rossi X-ray Timing Explorer All Sky Monitor (Swank, 1999), MAXI is the Monitor of All-sky X-ray Image aboard the International Space Station (Mihara et al., 2014), and Swift BAT is the Neil Gehrels Swift Observatory's Burst Alert Telescope (Krimm et al., 2013). The labeling is as follows: Yellow diamonds are known Be X-ray binaries, red crosses are supergiant high-mass X-ray binaries, orange crosses are supergiant fast X-ray transients, and purple boxes symbiotic X-ray binaries. Grayed out are sources that fall outside the WFM field of view during single pointings towards the Galactic Center. Source: Zhang et al. (2018).

2.3.3 Focusing Instruments

In addition to the LAD and WFM, eXTP consists of the SFA and the PFA. These instruments use a total of 13 X-ray grazing incidence Wolter I telescopes with a focal length of 525 cm and a maximal diameter of 510 mm. This kind of telescope is a combination of paraboloid and hyperboloid mirrors, of which X-rays are totally reflected when they have a grazing incidence. According to Singh (2011), the critical hitting angle depends on the density of the mirror material ρ and the wavelength of the incoming light λ and can be calculated with

$$\Theta_c \approx 5.6' \cdot \sqrt{\frac{\rho}{1\,\frac{\mathrm{g}}{\mathrm{cm}^3}}} \cdot \frac{\lambda}{1\,\mathrm{\mathring{A}}} \quad . \tag{2.2}$$

The mirrors, which are shells nested into each other to enlarge the effective area of the telescope, are coated with a metal that has a high density and therefore good reflection properties for low-energetic X-rays, for example iridium or gold (Sagdeo et al., 2010). The mirrors are made using a nickel electroforming approach, hence nickel replication, which has succesfully been used in BeppoSAX (Boella, G. et al., 1997), XMM-Newton (Lumb et al., 2012) and Swift (Burrows et al., 2005) and is planned to be used for eROSITA (Merloni et al., 2012), the ART-XC telescopes (Pavlinsky et al., 2008) of the Spectrum-Roentgen-Gamma astrophysical mission, and the IXPE polarimetric mission (Weisskopf et al., 2016). In this procedure, nickel mirror shells are electroformed in an electrolytic bath onto machined and superpolished aluminum mandrels. Once the mirror shells reach the desired thickness, they are released by differential thermal contraction (Ramsey, 2005). Since the focal length of an X-ray mirror increases with the energy of the incoming light, only energies up to 15 keV can be observed due to limitations in the telescope size. Specifications of the optics used for the SFA and PFA are shown in Table 2.3.

Table 2.3: The main specifications of the optics used for the SFA and the PFA. The specifications are given for one telescope. Source: Zhang et al. (2018).

Parameter	Specification
Energy range	0.5-10 keV
Collective area	$\geq$ 900 cm^2 at 2 keV; $\geq$ 550 cm^2 at 6 keV
Field of View	$\geq$ 12 arcminutes
Angular resolution (SFA)	1 arcminute
Angular resolution (PFA)	30 arcsec at 6 keV
Focal length	5.25 m
Maximal diameter of mirror shells	510 mm

The Spectroscopic Focusing Array

With its nine Wolter I grazing incidence telescopes that offer an effective area of ~7400 cm^2 at 2 keV and a field of view of 12 arcmin in diameter, the SFA is responsible for spectral-timing observations in the $0.5 - 10$ keV energy range. These observations have a time resolution of 10 µs, an energy resolution of <180 eV at 6 keV and an angular resolution of <1 arcmin. Each telescope consists of a thermal shield that holds the working temperature of the mirrors stable at (20 ± 2) °C, 19 SDDs, and a mirror module with an electron deflector attached to the bottom to reduce the particle background. A schematic of the SFA is shown in Figure 2.15.

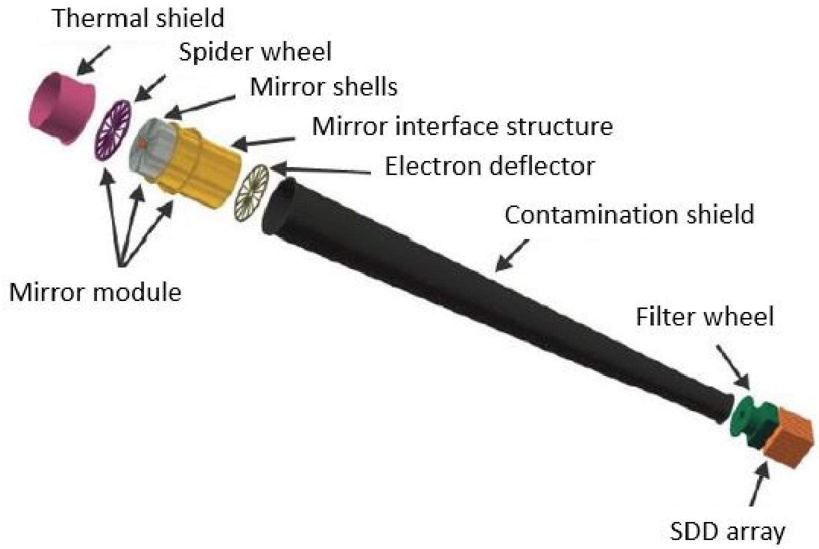

Figure 2.15: Schematic of the SFA. Source: Zhang et al. (2018).

The SFA electronics consists of the detectors, pre-amplifiers, analog-to-digital converters (ADCs) and an FPGA. After the detector signal has passed through the pre-amplifier, shaping and peak-holder, it reaches the ADC, from where the digital signal is sent to the FPGA. There, the data is packed into packets and passed on to the platform of the spacecraft. The focal plane detector (Figure 2.16a) consists of 19 SDDs, each with an area of 26.6 mm^2 for a total of 5 cm^2 detecting area. They have a hexagonal shape with a side length of 3.2 mm and a thickness of 450 µm. The central detector located at the focal position has its own ADC, while the other 18 SDDs are divided into three groups of which each has one ADC with multiplexers. Above the detector, a metal mask is attached to cover the gaps between the SDDs, decreasing the ratio of split events at the SDD edges. The detectors will operate in the temperature range of $-100\,°C$ to $-80\,°C$ to mitigate the effects of particle damage due to protons, and to reduce dark current[20] due to electrons that have a thermal energy of $E_{\text{therm}} = k_B T$, where k_B is the Boltzmann constant, and can be thermally excited into the conduction band of the detector. The temperature will be held stable to $\pm 5\,°C$ via heating compensation, for example by a proposed active method that uses a helium pulse tube and

[20] Dark current is produced although no photons hit the detector when electrons and holes are randomly generated by thermal excitation within the depletion region.

loop heat pipes[21].

The background during observations is reduced by an electron deflector, a magnetic system located underneath the mirror module that diverts soft electrons (electrons with energies of 300 kV or lower), multi-layer composites glued around the detector and a baffle above the filter wheel that supresses visible and X-ray stray light.

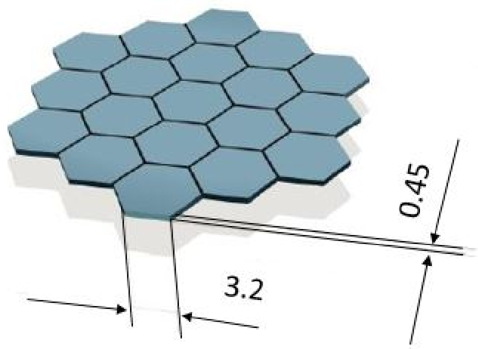

(a) Focal plane of the SFA.

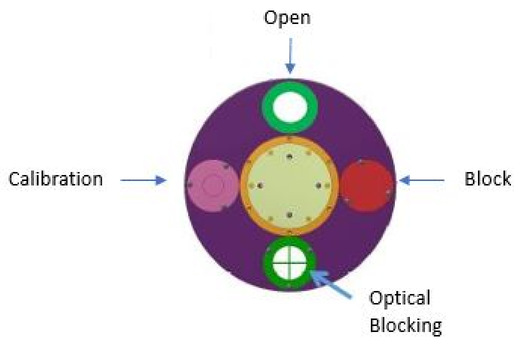

(b) Filter wheel of the SFA.

Figure 2.16: The SFA focal plane is shown in 2.16a. Each SDD has a side length of 3.2 mm and a thickness of 0.45 mm. 2.16b shows the filter wheel with the possible positions. These are, from the top in an anti-clockwise fashion: the open position for ground testing and observation of weak sources; the calibration, where an Fe-55 radioactive source is moved in front of the detector; optical blocking, where a polyimide and aluminum film are used to block out visible and UV light and prevent contamination of the detector; closed filter, where a metal sheet is rotated above the detector to measure the internal background and to prevent any damages to the detector. Source: Zhang et al. (2018).

The filter wheel (Figure 2.16b) mounted above the detector has four operational modes depending on the positions it is set to. The first possibility is the Open Filter, which is used for both ground tests and for observing weak sources during the mission.

[21] This structure is called a cryocooler and, for example, is used in the James Webb Space Telescope. The primary piece, the heat pump, consists of two parts: a preecooler using helium gas as a working fluid, and a high-efficiency pump that circulates helium gas as refrigerant previously cooled by conduction with the precooler. Using pulse tubes that acoustically exchange heat with a regenerator, the precooler, consisting of a two-cylinder horizontally-opposed pump, cools the helium gas. The high-efficiency pump, also a two-cylinder horizontally-opposed piston device, circulates a separate batch of helium gas. This primary piece is connected to plumbing within a cylinder the size of a coffee can. There, the cooled helium refrigerant passes through an opening with a diameter of less than 1 mm, which leads to an expansion and the final cooling. The helium gas with the final temperature then passes through tubes attached to a metal block located at the detector backside, where the heat is exchanged (NASA, 2018).

The second possibility is the on-orbit calibration mode, during which an Fe-55 radioactive source is moved in front of the detector to calibrate the instrument. The third mode is the optical blocking, which not only can block out visible and UV light with a 400 nm polyimide and 200 nm aluminum film, but also can prevent detector contamination. The last possibility is the closed filter mode, during which a metal sheet can be rotated in front of the detector in order to measure the internal background and to prevent any damage that can occur during launch or particle damages during solar events, such as solar flares.

The Polarimetry Focusing Array

The PFA uses four Wolter I telescopes to conduct spatial, energy and time resolved X-ray imaging polarimetry in the energy range of $2 - 8$ keV with a high sensitivity. By being the only instrument onboard the eXTP mission with an imaging capability better than 1 arcmin, the PFA can help to distinguish between different sources and therefore reduce source confusion. The required angular resolution is <30 arcsec and the optics are similar to the one of the SFA. However, instead of using SDDs, the PFA uses a Gas Pixel Detector (GPD) as a focal plane polarimeter.

The GPD that has an energy resolution of $15-20$ % at 6 keV consists of a gas chamber filled with dimethylether and is sealed with a 50 µm thick beryllium entrance window. A schematic of the GPD is shown in Figure 2.17. Dimethylether is chosen because, as it is typical in gases with a low proton number (low Z gas), it has a high stopping-power/scattering ratio and produces longer electron tracks than high Z gases. After absorbing the incident X-rays, the gas emits photoelectrons, whose emission angle is a key parameter to be measured since it entails information about the polarization of the incident X-rays. The emission angle can be found by reconstructing the 2D ionization track of the photoelectron within the chamber. Examples of electron tracks are shown in Figure 2.18. The end of the track is distinguishable by a larger release of charge. The direction of the photoelectron emission is found by looking for the principal axes of the charge distribution measured on the pixels. The two orthogonal directions give the maximal and minimal second momentum of the charge distribution, while the major principal axis is the photoemission direction (Bellazzini et al., 2003).

Secondary electrons that were ionized by the initial photoelectron are moved towards the anodes by the drift field, which has a strength of $\sim 2\,\frac{\mathrm{kV}}{\mathrm{cm}}$. By multiplying the number of electrons by a gain factor of a few hundreds, the Gas Electron Multiplier (GEM) that is attached above the anodes makes measurements with a sufficient signal-to-noise

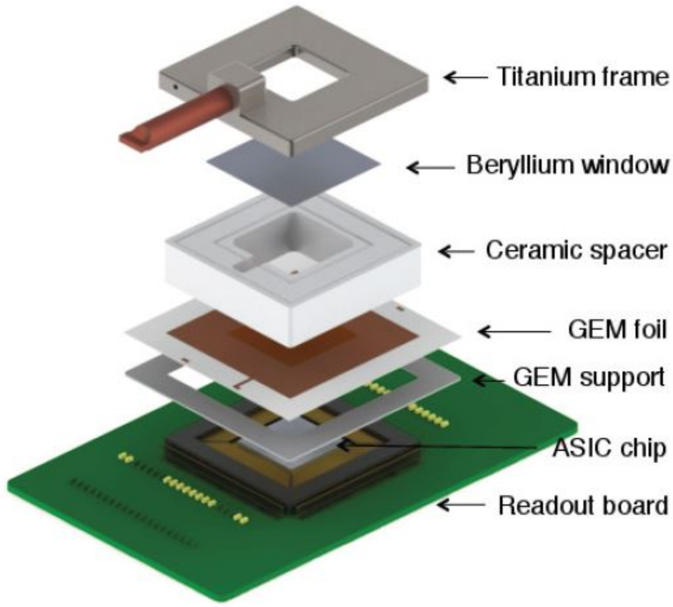

Figure 2.17: Exploded view of the Gas Pixel Detector used in the PFA. Underneath a Beryllium window and a ceramic spacer, the Gas Electron Multiplier is located. It enhances the electron signal to produce a sufficient signal-to-noise ratio. The readout is performed by an ASIC at the bottom of the detector. Source: Zhang et al. (2018).

ratio possible. The gain factor is adjustable by changing the high voltage across the top and bottom layer of this multiplier. The detector readout is performed by an ASIC chip that has the size of the sensitive detector area ($1.5\,\mathrm{cm}^2 \times 1.5\,\mathrm{cm}^2$), is pixelated to have a pitch of 50 µm and collects as well as measures the multiplied charges.

The sensitivity of the polarimeter is the minimum detectable polarization (MDP) described by (Muleri et al., 2008):

$$\mathrm{MDP} = \frac{4.29}{\mu \cdot \epsilon \cdot F}\sqrt{\frac{\epsilon \cdot F + B}{S \cdot t}} \quad , \tag{2.3}$$

which for a case where the background is of no importance[22] becomes

$$\mathrm{MDP} = \frac{4.29}{\mu\sqrt{S \cdot t \cdot \epsilon \cdot F}} \quad . \tag{2.4}$$

[22]Pacciani et al. (2003) states that the X-ray diffuse background on one steradian at 1 keV is about the same level of the Crab Nebula. Because of this, focal plane polarimeters are source dominated down to very small fluxes and the background can be neglected.

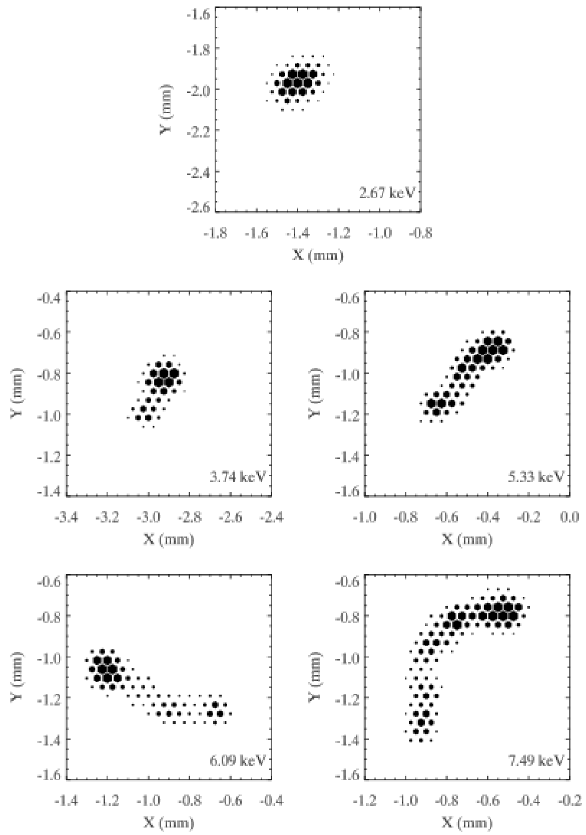

Figure 2.18: Example electron tracks measured for incident X-ray photons with different energies. The end of the tracks is distinguishable by a larger release of charge. Source: Li et al. (2015).

In Equations (2.3) and (2.4), F is the source and B is the background flux in a selected energy range, ϵ is the detector efficiency, S is the collecting area, t is the exposure time, 4.29 is the 99 % confidence level, and μ is the modulation factor. The modulation factor can be found by looking at the angular distribution of a source. As Bellazzini et al. (2003) states, for unpolarized sources, this distribution is flat. For polarized sources however, the angular distribution peaks around the polarization angle and is modulated by

$$C(\phi) = D + E \cdot cos^2(\phi - \phi_0) \quad . \tag{2.5}$$

Here, $C(\phi)$ is the modulation, D is a constant term originating from the randomization that is induced by Coloumb scattering, E is a constant, the cos^2 term stems from the cross-section of the photoelectric effect, ϕ is the photoelectron emission angle, and ϕ_0 is the position angle of polarization. Since the operating principle of the GPD is based on the photoelectric absorption of gas and the photoelectrons are mainly emitted along the absorbed photons' electric field, which is also the direction of polarization, the emission of photoelectrons produced by linearly polarized radiation is modulated with an amplitude proportional to the degree of polarization (Muleri et al., 2008). For 100 % polarized photons, the amplitude of the modulation described in Equation (2.5) is called the modulation factor μ, which, according to (Bellazzini et al., 2003), can be calculated with:

$$\mu = \frac{C_{max} - C_{min}}{C_{max} + C_{min}} = \frac{E}{2D + E} \quad . \tag{2.6}$$

The modulation factor represents the response of an instrument to a fully polarized photon beam, meaning that a higher modulation factor corresponds to the capability to detect weaker polarized signals (Bellazzini et al., 2013). As described by Muleri et al. (2008), the modulation factor increases when the resolution and reconstruction of the photoelectrons' emission direction improve. For high energy photons, the photoelectron tracks get longer, therefore increasing the modulation factor. Next to the modulation factor, the efficiency ϵ is a primary parameter for the polarimeter's sensitivity. Because the GPD will be located at the focus of the X-ray optics, Equation (2.4) is used to calculate the minimum detectable polarization, which is inversely proportional to the quality factor $\mathrm{QF} = \mu\sqrt{\epsilon}$ (Muleri et al., 2010). According to Pacciani et al. (2003), the quality factor is used to compare different polarimeter configurations and, as Muleri et al. (2008) states, should be selected such that it is maximized within a selected energy range. To improve the modulation factor of a polarimeter, the nuclear scattering should be reduced by using a low Z gas. However, to improve the polarimeter efficiency, the atomic number should be increased, leading to the usage of a high Z gas. The maximization of the quality factor is therefore a trade-off between the modulation factor and the efficiency. An example for the interdependence of efficiency, modulation factor and the quality factor can be seen in Figure 2.19.

Looking at the quality curve and the total effective area for the four PFA telescopes in Figure 2.20, it can be seen that the latter peaks at 2 keV, while the quality curve peaks at 3 keV because of the relationships between modulation factor, energy and detector efficiency discussed above.

[23] Monte Carlo experiments are algorithms that use random samples to obtain results.

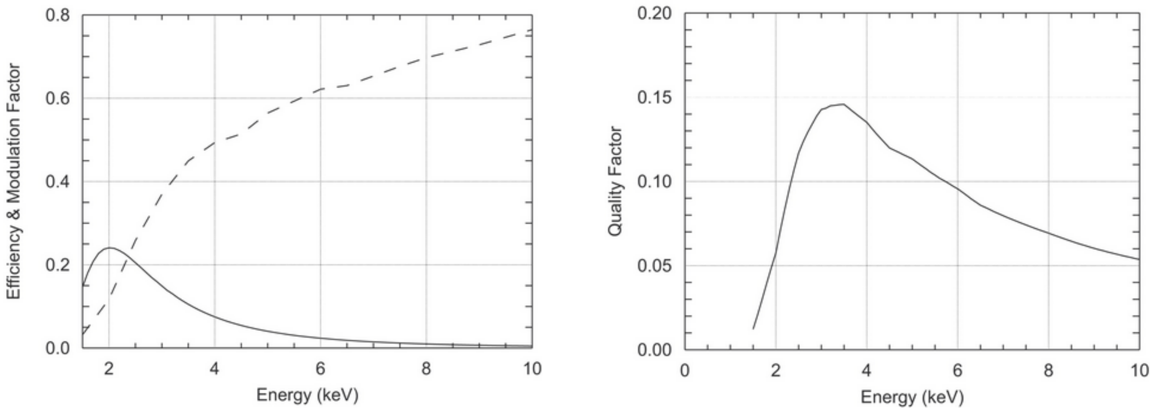

(a) Efficiency and modulation factor for a Gas Pixel Detector.

(b) Quality factor for a Gas Pixel Detector.

Figure 2.19: Efficiency, modulation factor and quality factor for a Gas Pixel Detector. The solid line in 2.19a represents the efficiency of a Gas Pixel Detector filled with 20 % Helium and 80 % dimethylether. The dotted line in 2.19a shows the modulation factor for the same detector and was determined with a Monte Carlo code[23]. 2.19b depicts the quality factor for the same detector as in 2.19a. The peak of the sensitivity is reached at approximately 3 keV. Source: Muleri et al. (2008).

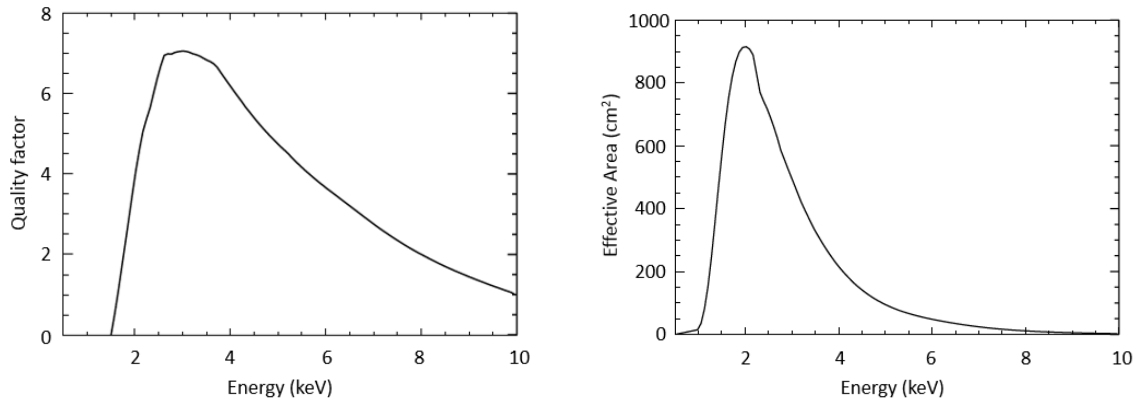

(a) Quality Curve for the four PFA telescopes.

(b) Total effective area for the four PFA telescopes.

Figure 2.20: The quality curve (2.20a) and total effective area in combination with the detector (2.20b) for the four PFA telescopes. The quality curve peaks at approximately 3 keV due to the relationship between modulation factor, energy and detector efficiency. The total effective area of the telescopes peaks at 2 keV. Source: Zhang et al. (2018).

3 Silicon Drift Detectors for eXTP

While the PFA uses a Gas Pixel Detector as a focal plane detector, the SFA, the LAD and the WFM make use of a different detection technique: Silicon Drift Detectors. These detectors are frequently used in astrophysics because of their X-ray imaging and spectroscopic characteristics as well as their large area in combination with a very good energy resolution. Other benefits for their astrophysical use are their low weight ($\sim 1\,\frac{\mathrm{kg}}{\mathrm{m}^2}$), volume, power and cost (Campana et al., 2011). In this chapter, the general SDD working principle will be explained (Section 3.1) and the configurations employed in the SFA, LAD and WFM will be described (Section 3.2).

3.1 Working Principle

In 1983, Emilio Gatti and Pavel Rehak proposed a new kind of detector, the Silicon Drift Chamber (Gatti and Rehak, 1984). This chamber was a variation of the gas-proportional counter used for position sensing. According to Strüder et al. (1998), the working principle of an SDD is based on sideward depletion, in which a large semiconductor wafer, for example silicon, is fully depleted by a small anode. The working principle of both a round and a rectangular SDD is shown in Figure 3.1. In the following, the working principle for a SDD will be explained according to PNDetector (2013). For a round SDD, a rectangular SDD, or SDDs of other forms, the shape of the field strips and therefore of the drift potential is different, however, the overall working principle is the same for all kinds of SDDs.

On the side where radiation enters the n-type silicon bulk, the *back side*, a homogeneous $\mathrm{p}^+ - \mathrm{n}$ junction is located, while the opposite side has a structure of p^+ field strips adjusted to the form of the SDD. A negative voltage is applied to the backside, while the field strips have an increasingly negative voltage, leading to a potential field distribution inside the detector such that the readout anode is located at the point of minimum potential energy for electrons. These electrons, forming a photoelectron cloud, are created due to ionization loss when a photon interacts with the detector.

The electron cloud drifts towards the anode due to the potential field distribution.

In some cases, the spectroscopic performance of an SDD is improved by integrating the first amplification step directly onto the sensor, for example with a JFET transistor[1] as shown in Figure 3.1. In order to achieve the signal amplification, the anode is connected to the transistor gate by a small metal strip to reduce unwanted noise.

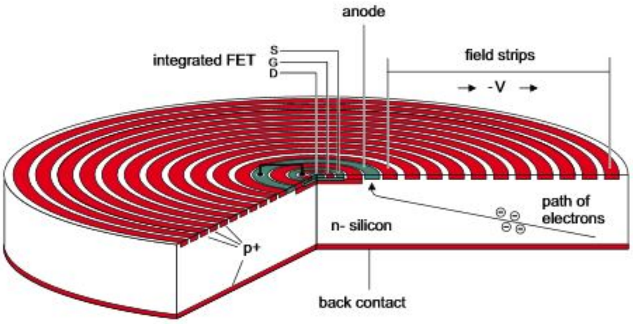

(a) Round Silicon Drift Detector.

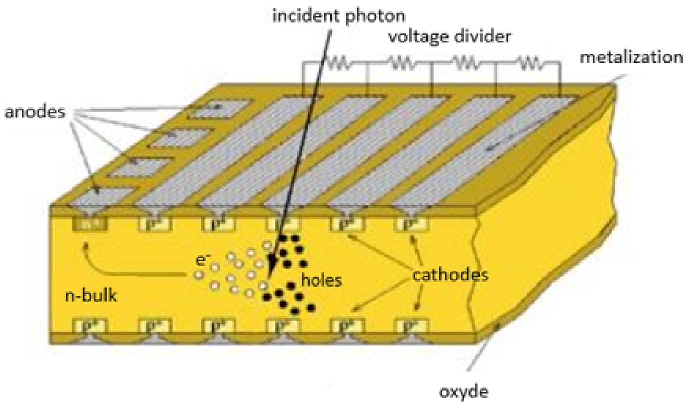

(b) Rectangular Silicon Drift Detector.

Figure 3.1: The working principle of a round and a rectangular SDD. The round SDD shown in 3.1a is covered by circular p^+ drift rings on the one and a homogeneous $p^+ - n$ junction on the other, the photon entrance, side. By applying the appropriate voltages, a drift field is created, due to which the electron cloud moves to the anode. 3.1b shows the absorption of a photon in the silicon bulk of a rectangular SDD. Photons that hit the detector produce an electron cloud that moves towards the anodes due to the drift field. Source: PNDetector (2013) and Brandt et al. (2014), respectively.

[1]Junction Gate Field-Effect transistor, see Grundmann (2016) for details.

3.2 The eXTP Silicon Drift Detectors

As can be seen in Figure 2.16a, the detectors of the SFA have a hexagonal shape with a side length of 3.2 mm and a thickness of 0.45 mm. Each detector has an active area of 26.6 mm^2. Having 19 SDDs as focal plane detector, each of the nine SFA telescopes has an active detection area of 505.4 mm^2 (Zhang et al., 2018). Each detector has one anode located at the center of the tile and a drift field that is created such that it surrounds the anode in a hexagonal shape.

The SDDs employed for the LAD and the WFM in the eXTP mission were originally developed for ALICE (A Large Ion Collider Experiment, The ALICE Collaboration et al. (2008)), an experiment located at the Large Hadron Collider at CERN. The ALICE-D4 SDD (Figure 3.2), which is used in the Inner Tracking System, has a size of 7.53 cm $\times$ 8.76 cm and is able to find the impact coordinates of the ionizing particles with a spatial resolution better than 30 µm in one dimension. Each ALICE-D4 SDD has a sensitive area of 75.7 mm $\times$ 70.0 mm = 53 cm^2 and is electrically separated into two halves, each housing 256 anodes with a pitch of 294 µm. Due to this separation, the maximum drift length is 35 mm. By setting the maximum drift voltage to $V_{drift} = -1300\,V$, the drift field across the depleted zone becomes $360\,\frac{V}{cm}$ (Campana et al., 2011). A comparison of the ALICE-D4 SDD and the SDDs employed in the eXTP mission can be found in Table 3.1.

Since the detector is electrically divided into two halves, the maximum drift distance for the electron cloud is half the detector width. In the following part, the focus will be on only one of the halves. All formulas can be applied to the other half as well.

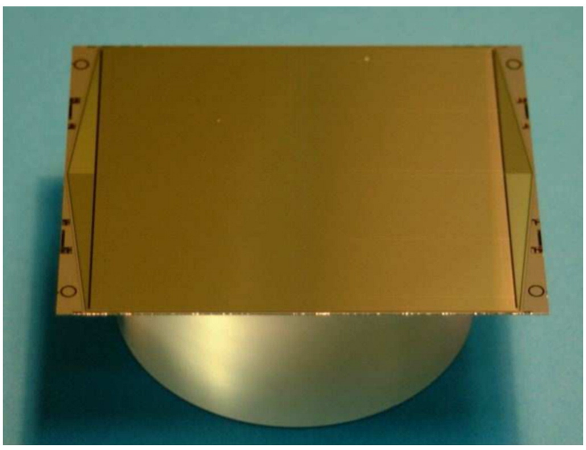

Figure 3.2: The ALCE-D4 Silicon Drift Detector. Source: Campana et al. (2011).

Table 3.1: Comparison of the ALICE-D4 SDD and the SDDs employed in the eXTP mission. Since the SFA SDDs have a hexagonal shape with only one anode in the middle, the respective information was adjusted.

Parameter	ALICE	SFA	LAD	WFM
Si thickness	300 µm	450 µm	450 µm	450 µm
Si tile geometric size	7.53 cm × 8.76 cm	side length: 3.2 mm	12.0 cm × 7.2 cm	77.4 mm × 72.5 mm
Si tile active area	53 cm^2	26.6 mm^2	76 cm^2	45.57 cm^2
Anode pitch	294 µm	N/A	970 µm	145 µm
Number of anodes per half	256 anodes	1 anode per detector	112 anodes	448 anodes
Maximum drift length	35 mm	3.2 mm	35 mm	35 mm

Due to diffusion, the electron cloud drifting towards the anodes increases in size. According to Campana et al. (2011), the shape of the cloud can be described by a Gaussian shape:

$$\rho(\vec{r},t) = \frac{q}{2\pi\sigma^2(t)} \cdot \exp\left(\frac{(\vec{r}-\vec{r}_0(t))^2}{2\sigma^2(t)}\right) \quad , \tag{3.1}$$

where ρ is the charge density, $\vec{r}_0(t)$ is the cluster centroid, q is the elementary charge and $\sigma(t)$ is the charge cloud size. Using the diffusion coefficient

$$D = \frac{k_B T}{q} \cdot \mu_e = \frac{k_B T \cdot v_D}{qE} \quad , \tag{3.2}$$

in combination with the drift time

$$t = \frac{x_D}{v_D} \tag{3.3}$$

the cloud size upon reaching the anodes can be calculated:

$$\sigma(t) = \sqrt{2 \cdot Dt + \sigma_0^2} = \sqrt{2\frac{k_B T \cdot x_D}{qE} + \sigma_0^2} \quad . \tag{3.4}$$

In equations (3.2), (3.3) and (3.4), $\mu_e = \frac{v_D}{E}$ describes the electron mobility with the drift velocity v_D and drift field E, k_B is the Boltzmann constant, T is the temperature, q is the elementary charge, x_D is drift distance, and σ_0 is the initial cloud size. Assuming a temperature of $T = 300\,\mathrm{K}$ and a drift field of $E = 360\,\frac{\mathrm{V}}{\mathrm{cm}}$, Equation (3.4) becomes

$$\sigma(t) = \sqrt{1.39 \cdot x_D + \sigma_0^2} \quad , \tag{3.5}$$

with x_D and σ_0^2 being in µm. In silicon, σ_0^2 corresponds to the range of a 50 keV electron within the material, which is ∼20 µm. Comparing the initial cloud size of ∼20 µm with the cloud size upon reaching the anodes of multiple hundred µm (see Figure 4.4), the initial cloud size becomes insignificant. For this reason, σ_0^2 can be ignored from now on.

As described in Campana et al. (2011), the reconstruction of the initial photon position in anode direction y_0 and in drift direction x_0 is done by fitting the collected charge at the anodes. Since the coordinate system is chosen in a way such that the anodes are located at the zero coordinate, the drift distance x_D is equal to x_0. The cloud reaching the anodes has a Gaussian shape according to Equation (3.1), with an area equal to the total charge and a mean value $\mu = y_0$. Each anode collects a charge described by

$$Q_i = K + \frac{Q_{tot}}{2} \cdot \left[\mathrm{erf}\Big(\frac{y_i - y_0 + p/2}{\sigma\sqrt{2}}\Big) - \mathrm{erf}\Big(\frac{y_i - y_0 - p/2}{\sigma\sqrt{2}}\Big) \right] \quad , \tag{3.6}$$

where K is the baseline level due to common-mode noise[2] which changes from event to event, Q_{tot} is the total cloud charge, y_i is the center position of the i^{th} anode relative to y_0, p is the anode pitch and erf is the error function. By fitting Equation (3.6) simultaneously over all anodes, y_0 and the charge cloud size can be found. The initial photon position in drift direction x_0 cannot be determined directly because no information about the time of photon absorption is available, meaning that the drift time cannot be calculated. However, by fitting Equation (3.6) to the measured charge distribution on the anodes and finding the charge cloud size, the drift distance x_D, and therefore the initial photon position in drift direction x_0, can be found by solving Equation (3.5).

Campana et al. (2011) tested this method for the ALICE-D4 SDD and compared it with simulations, in which a Monte Carlo code was employed to create a photon at a previously set or random position (x_0, y_0), from which an electron cloud with a Gaussian shape $\mu = y_0$ and size σ calculated from x_0 was constructed. The results of this test are shown in Figure 3.3. It can be seen that the reconstruction from both real data and the simulations are in agreement with each other. Therefore, the method is suitable to reconstruct the initial photon interaction position.

The LAD and WFM SDDs are optimized ALICE-D4 detectors, originally for the use onboard the LOFT mission. They have a large photon collecting area, which is read out by a set of low-capacitance anodes. When the XTP and LOFT missions[3] were

[2] Common-mode noise at the anode level is created by a voltage step on the grid that surrounds the anodes. A voltage step of 0.65 mV creates a charge on each anode that is equivalent to that created by a 1 keV photon and is equal for every anode. At the ASIC level, common-mode noise is created by fluctuations on the power supply that enter the chips in multiple points, but also originates from bias voltages and currents derived from the power supply line. By calculating an subtracting the median signal of all the channels in one ASIC, the common-mode noise can be removed from the anode signals in the BEE.

[3] See Chapter 2

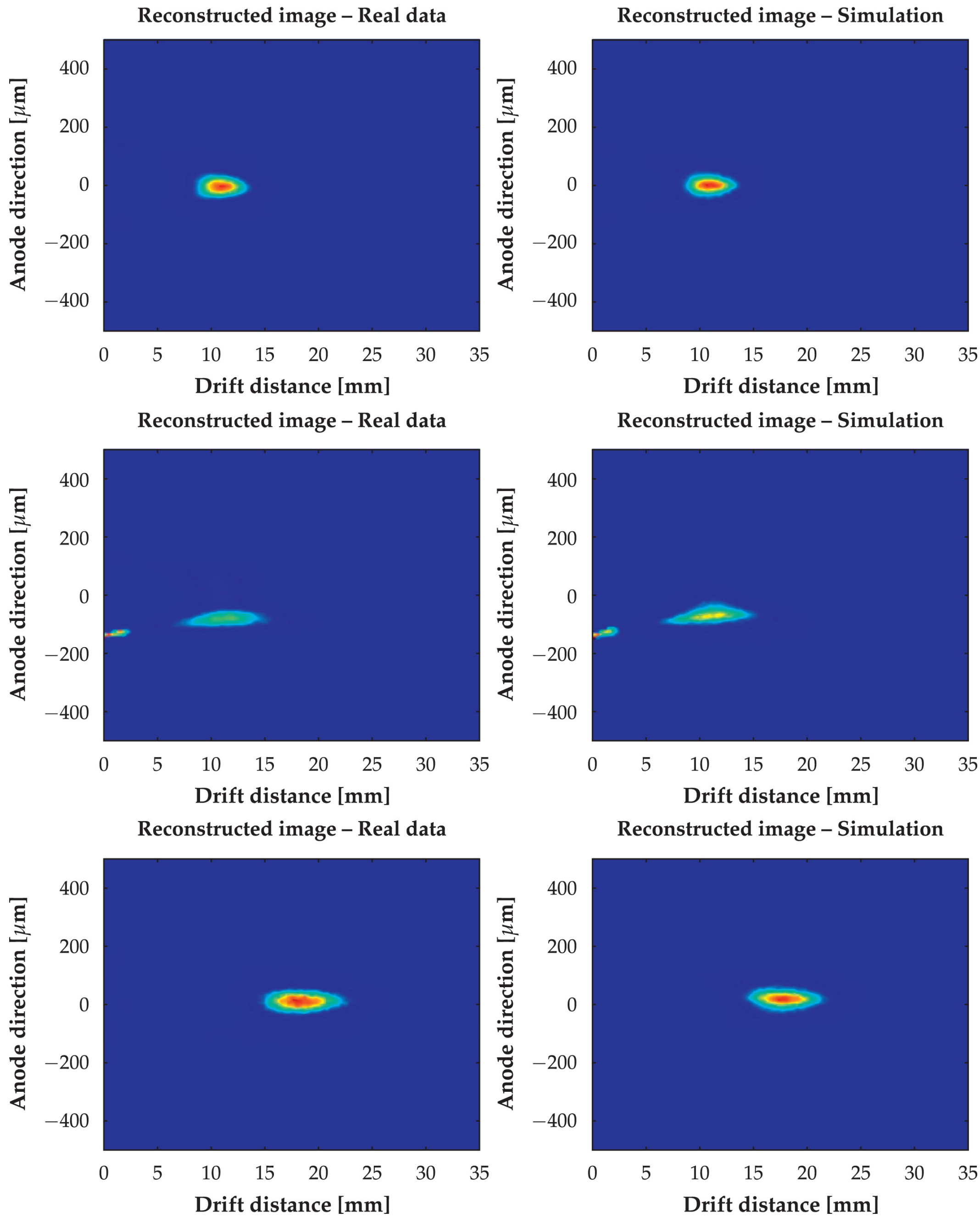

Figure 3.3: Results of the photon reconstructions based on fitting Equation (3.6) simultaneously for all anodes. The left column shows the reconstruction from real data (a 30 minute integration with a 4.5 keV monochromatic beam of $\sim$ 100 µm FWHM), the right column depicts the reconstruction from simulations of a Gaussian beam with $\sim$ 100 µm FWHM. From top to bottom, the beams are centered at x_0 = 10 mm and y_0 = 0 mm, x_0 = 10 mm and y_0 = - 75 µm, x_0 = 18 mm and y_0 = 10 µm, respectively. Source: Campana et al. (2011).

merged to become eXTP, the LOFT SDD design was adopted. Both the LAD and WFM detectors are of rectangular shape with sizes of 12.0 cm × 7.2 cm and 77.4 mm × 72.5 mm, respectively. Both detectors have a thickness of 0.45 mm. The LAD SDD has an active detector area of $10.85\,\text{cm} \times 7.0\,\text{cm} = 76\,\text{cm}^2$, resulting in a maximum drift length of 35 mm. The two halves of the detector each house 122 anodes with a pitch of 970 µm (Zhang et al., 2018). According to Feroci et al. (2018), this pitch was chosen to reduce the power consumption in comparison to the ALICE-D4 detector. The WFM detector has an active area of $65.1\,\text{mm} \times 70.0\,\text{mm} = 45.57\,\text{cm}^2$ and, just as the ALICE-D4 and the LAD SDDs, a maximum drift length of 35 mm. Each of the detector halves has 448 anodes that are separated by 145 µm (Brandt et al., 2014). As for the ALICE-D4 SDD, the maximum voltage for both the LAD and WFM SDDs is set to $V_{\text{drift}} = -1300\,\text{V}$, resulting in a drift field of $360\,\frac{\text{V}}{\text{cm}}$. The drift velocity of $\sim 5\,\frac{\text{mm}}{\mu\text{s}}$ leads to a maximum drift time of $\sim 7\,\mu\text{s}$. Due to this drift time, the photon arrival time can only be determined with a precision of 7 µs (Zhang et al., 2018). Unlike for the WFM, where source positions are crucial and therefore the initial photon position needs to be reconstructed, the LAD is used for spectral timing studies and a position reconstruction is not necessary. The reconstruction resolution for the WFM SDD in both positions and the energy is shown in Figure 3.4. For energies at 6 keV, the energy resolution is better than 300 eV, while the position resolution in drift direction is better than 8 mm and in anodic direction better than 60 µm (Hernanz et al., 2018). For the LAD, the spectral resolution at 6 keV is up to 200 eV FWHM (Feroci et al., 2018).

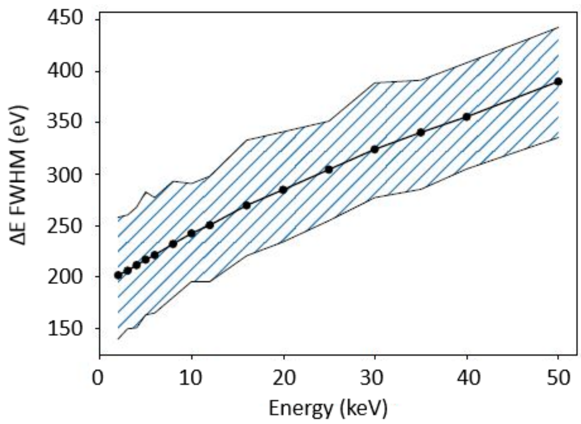

(a) Energy resolution.

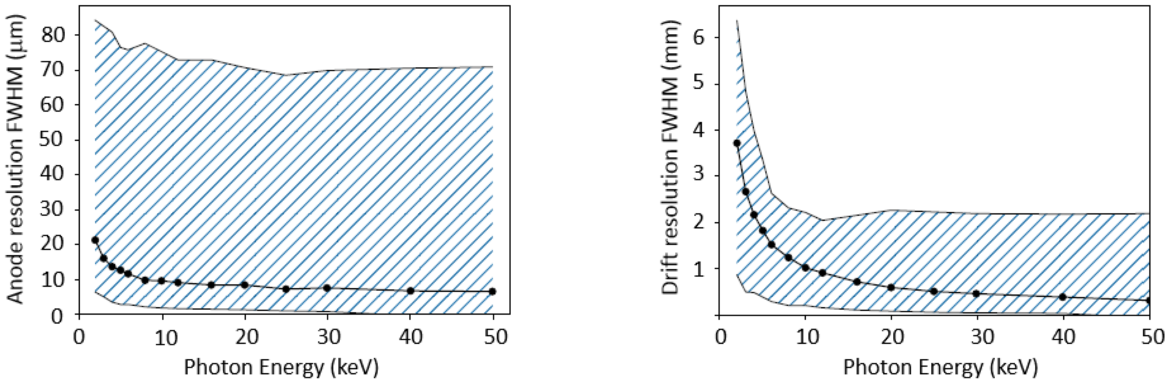

(b) Reconstruction resolution in anodic and drift direction.

Figure 3.4: Energy resolution (3.4a) and reconstruction resolution in drift and anodic direction (3.4b) for the WFM SDD as functions of the photon energy. For 3.4a, the shaded area shows the range of energy resolution for each photon energy, whereas the shaded area in 3.4b is the range of spatial resolution inside the detector channel. For both 3.4a and 3.4b, the filled circles show the averaged values on the whole SDD channel. Source: Campana et al. (2011).

4 The Detector Simulator

In this Master's thesis a detector simulator for the WFM SDD, consisting of both a software part running on a PC, and a hardware device, was created. In order to simulate the WFM SDD, data are generated on the PC and then transmitted to an FPGA, on which the data can then be stored. The purpose is to turn on the programmed FPGA, load the generated data onto it and finally release photon interaction event data in random time intervals. The recipient of the data is a read-out electronics, currently developed at the Institute for Astronomy and Astrophysics Tübingen (IAAT), that can be tested that way. The overall data flow is shown in Figure 4.1.

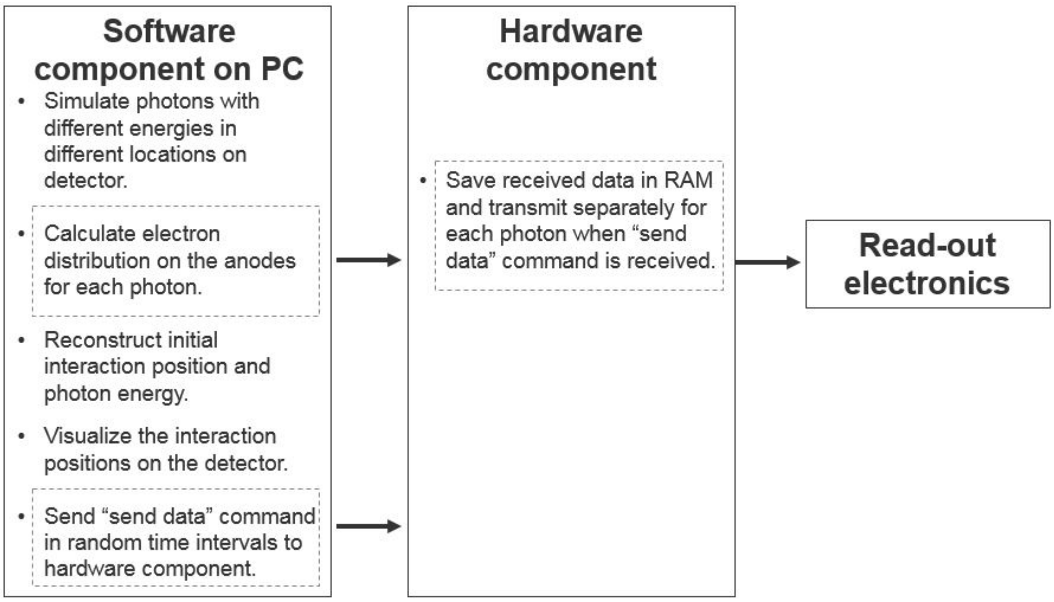

Figure 4.1: Data flow of the detector simulator. The software component is responsible for simulating photons with different energies in different locations on the detector and for calculating the electron distribution on the anodes for each photon. This data are not only sent to the hardware component, but also used to again reconstruct the initial interaction position and photon interaction. From this reconstruction, the interaction positions on the detector are visualized. On the hardware component, the data is saved in a Random Access Memory (RAM) and transmitted to the read-out electronics once the "send data" command from the software component is received.

The data that are generated on the PC consist of the anode positions and the respective number of electrons reaching them according to Equation (3.6). Therefore, the requirements for the software part of the simulator are the following:

1. Simulate photon interactions in different locations on the detector.
2. The energy of the photons is chosen according to the Crab Nebula spectrum, a known standard candle in the X-rays and therefore representative of a typical photon energy distribution for an X-ray source.
3. For each photon, the electron distribution on the anodes has to be calculated according to Equation (3.6), since this is the only information that the simulator will deliver to the read-out electronics.
4. The anode positions and electron distribution have to be translated to the binary system in order to have the correct data format.
5. Transmit the binary data to the FPGA.
6. In software, reconstruct the initial interaction position and photon energy from the anode positions and respective electron numbers in order to check the correct functioning of the tested read-out electronics.
7. Visualize the interaction positions on the detector based on the reconstructed data.
8. Save all results in files.
9. Send a "send data" command to the FPGA in random time intervals once the data is stored on the FPGA.

The hardware, which is the recipient of the data created in the software part of the simulator, consists of an FPGA that is programmed and encased in an aluminum box such that it is ready for use once the power switch on the box is turned on. In order to achieve this, the FPGA is programmed as follows:

1. The binary data sent from the software part of the simulator are saved in an onboard memory. The sending and saving of the binary data has to be the first step once the FPGA is turned on because the onboard memory is wiped once the FPGA is powered off.
2. The saved data are transmitted to the connected electronics once the "send data" command is received. It is important that each time only the data for one photon are sent to the electronics in order to simulate single photon events.

In the following, the software and hardware components of the detector simulator will be described in more detail.

4.1 The Software Component of the Simulator

The software component of the simulator was written in Python 3.6[1] on a Windows7 machine. The codes written in the scope of this thesis were executed using Jupyter Notebooks[2]. An exception was the sending of data to the FPGA, which was executed using the Windows Command Prompt. The software component of the simulator has three main tasks. The first one is to simulate the interaction of photons with the detector, the second one is to use this data to reconstruct the initial interaction position and photon energy as well as to visualize the locations of the photon interactions on the detector, and the third is to send the data and a "send data" command to the hardware component. As mentioned in Section 3.2, the SDD is electrically divided into two halves. As both halves are identical in their behavior, only one detector half will be simulated.

4.1.1 Interaction of Photons with the Detector

The aim of the first software module is to simulate the interaction of a number of photons with the WFM SDD (Figure 4.2). An object oriented programming approach was chosen for this module, creating the classes *Photon* and *Detector*, which are instantiated during the simulation. The *Photon* class calculates the number of electrons that the incoming photon produces within the silicon bulk. Since the creation of charges in the detector is a statistical process, the actual number of electrons is simulated by using a Gaussian distribution with a mean $\mu = N_{e^-,expected}$ and a standard deviation $\sigma = \sqrt{N_{e^-,expected}}$. The expected number of electrons $N_{e^-,expected}$ is calculated by

$$N_{e^-,expected} = \frac{E_{phot}(\mathrm{keV})}{E_{average}(\mathrm{keV})} \quad , \tag{4.1}$$

where $E_{average}$ is the average energy needed to create an electron-hole-pair, which for silicon is set to 3.6 eV in the simulation. For each photon, an individual detector is created using the *Detector* class. In this class, the number of electrons at the i^{th} anode

[1]Python can be installed from `www.python.org`. The description of available modules, including the ones used in this thesis, can be found at `www.docs.python.prg/3/py-modindex.html`.

[2]Jupyter Notebook is an open source web application that supports interactive data science and scientific computing in all programming languages. Information about the download, installation and the documentation for Jupyter Notebooks can be found at `www.jupyter.org`.

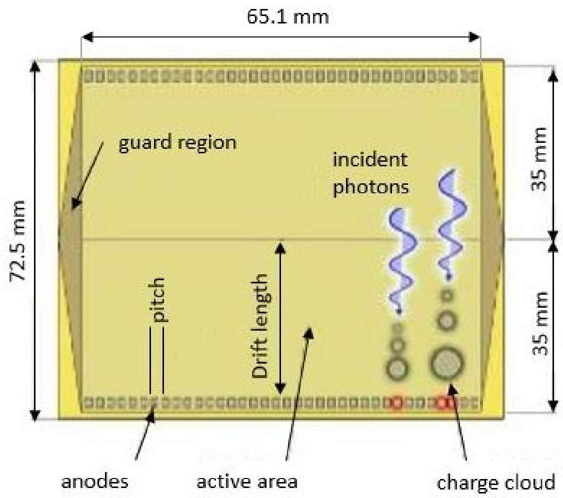

Figure 4.2: Illustration of the top view of the WFM SDD with the anodes at the top and the bottom. As described in Section 3.1, the SDD is electrically divided, which is implied by the horizontal line in the middle of the detector. Photons that hit the detector produce an electron cloud that moves towards the anodes, either the ones at the top or the ones at the bottom, due to the drift field. Source: Brandt et al. (2014)

is calculated according to Equation (3.6) with the addition of a Gaussian noise distribution with mean $\mu = 0$ and a standard deviation $\sigma = 3$. The reason for this addition is to include the variation of offsets and dark currents in the simulation. The charge cloud size needed for this calculation is also found within the *Detector* class. For this, Equation (3.4) is used. However, the result obtained with Equation (3.4) only describes the size of the charge cloud within the 68 % confidence level and therefore does not entail the whole charge cloud. Because a realistic charge cloud size is needed to obtain the correct number of electrons at the i^{th} anode, the result of Equation (3.4) is multiplied by six.

Depending on the scenario that should be simulated, the initial interaction positions and photon energies can be set in two ways:

1. All photons have the same initial interaction positions and photon energies.

2. All photons have different initial interaction positions and photon energies.

Since only half the detector is simulated, the incident position in drift direction ranges from 0-35,000 µm and the one in anode direction ranges from 0-65,100 µm, depending on the maximum drift length and the active detector size of the WFM SDD as mentioned in Table 3.1. The energy of the incoming photons is randomly chosen from a distribution following the Crab Nebula's spectrum. According to Kellogg (1971), the spectrum above 1 keV can be fitted with a power law of the form

$$\frac{dN}{dE} = KE^{-\beta} \frac{1}{cm^2 \cdot s \cdot keV} \quad . \tag{4.2}$$

As Kellogg (1971) states, for energies below 22 keV this fit becomes

$$\frac{dN}{dE} = 5 \cdot E^{-1.95} \frac{1}{cm^2 \cdot s \cdot keV} \quad , \tag{4.3}$$

while Manchanda et al. (1982) says that for energies above 22 keV,

$$\frac{dN}{dE} = 16.6 \cdot E^{-2.3} \frac{1}{cm^2 \cdot s \cdot keV} \tag{4.4}$$

is a suitable fit. Using these results, the spectrum as shown in Figure 4.3 can be obtained. Equations (4.2) and (4.3) are integrated between their respective boundaries (2 keV and 22 keV for Equation (4.2); 22 keV and 50 keV for Equation (4.3)) and normalized between the minimum and maximum energies to find the probability density function of the spectrum, according to which the inital photon energy is randomly chosen. The energy distribution of 100,000 photons based on the spectrum's probability density function is also shown in Figure 4.3.

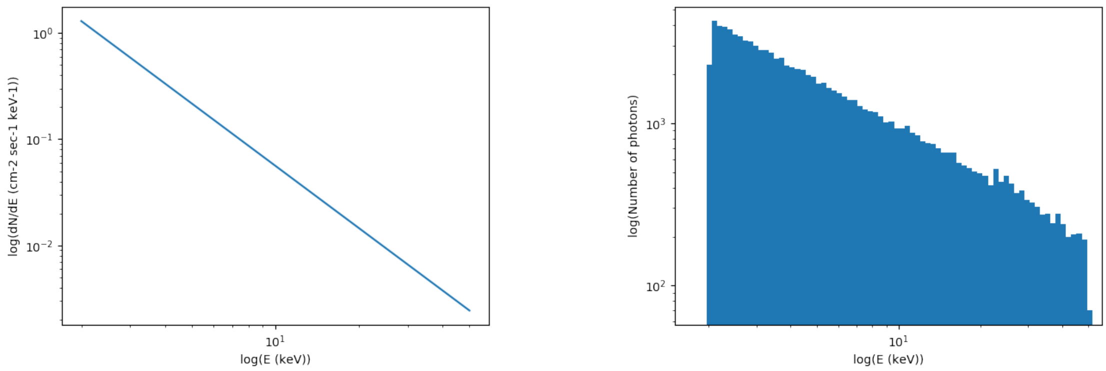

(a) The Crab Nebula spectrum in the energy range 2-50 keV on a logarithmic scale.

(b) The energy distribution of 100 000 photons in the energy range 2-50 keV.

Figure 4.3: The Crab Nebula spectrum (4.3a) and the energy distribution of 100,000 photons based on the spectrum's probability density function (4.3b) in the energy range 2-50 keV.

In order to use the *Photon* and *Detector* classes for multiple photons at a time, two functions were utilized. The first function, *simulation_charge_cloud_size*, creates a file that contains the photons' incident interaction position as well as the initial energy and the resulting charge cloud sizes at the anodes for each photon. This file is created as a comparison to the values that will be reconstructed in the reconstruction module of the software component and has no other use. An example of this file for five photons with different energies and initial interaction positions is shown in Figure 4.4. The second function, *simulation_charges_at_anodes* creates two files, which can be seen in Figure 4.5. The first file contains the anode positions within the detector and the respective number of electrons on the anodes, which is the only information that the simulated detector FEE sends to the read-out electronics and that will later be used to reconstruct the initial interaction positions and photon energies. Since, as mentioned above, the number of electrons at an anode is calculated according to Equation (3.6) with the addition of a Gaussian distribution with mean $\mu = 0$, the resulting number of electrons can be negative. In a future version of the simulator, this could be optimized by using a Rice distribution (Rice, 1945). The second file that is created by this function contains the same information as the first file, however in binary format. In order to obtain this format, the anode positions and respective number of electrons are converted into 16 bit and 32 bit strings, respectively, using the IEEE-754[3] conversion. These two strings are then merged into one string with a length of 48 bits and saved as such. This second file is the input for the FPGA. In future versions of the simulator it should be considered that the front end electronics include an ADC that records the number of electrons at the anodes by measuring the voltage signal at each anode and represents this number with an integer between 0 and 4095 in binary format.

Charge Cloud Size(um), 6 sigma	Energy(keV)	x_incidence (um)	y_incidence(um)
880.0667480746779	3.613593880949079	14992.595452317817	63561.737964510285
847.0254127910646	5.983016847732349	13887.96070293986	7861.547423526643
717.6045625227941	5.854039109045494	9968.182503939812	42313.39462255057
578.6407819999056	6.025635738104532	6481.323162862219	58596.98875012124
115.28238845189807	3.9204464176229323	257.2595642116593	9628.847986848303

Figure 4.4: The file containing charge cloud size for five photons with different energies and initial interaction positions, created by the *simulation_charge_cloud_size* function.

All files can be created such that either each photon gets its own file or all information for all photons is saved in three files (the first containing the incident positions, energies and charge cloud sizes, the second containing the anode positions and the number of electrons at the respective anodes, and the third containing the information of the second file in binary format). The first method might be used when a small number of photons interacts with the detector and single photons will be analyzed. The

[3] IEEE 754 is the standard for floating-point arithmetic in computer systems and was developed by the Institute of Electrical and Electronics Engineers (IEEE) (IEEE, 2008).

second method is useful when large numbers of photons are supposed to interact with the detector since only three and not three times the number of interacting photon files will be created. In the following description of the other modules, it is assumed that the information is saved with the second method.

Anode position (um),	Electrons at anode
145,	-4.288937380245173
290,	-5.390725940004063
435,	2.429280594555932
580,	-1.3803442734972493
725,	1.5316347118440032

(a) Anode positions and respective electron number for five anodes.

```
000000001001000111000000100010010011111011111010
000000010010001011000000101011001000000011010100
000000011011001101000000000110110111100101010101
000000100100010010111111101100001010111100011111
000000101101010100111111110001000000110010011011
```

(b) Binary format of anode positions and respective electron number for five anodes.

Figure 4.5: Anode positions and respective electron number in normal (4.5a) and binary (4.5b) format. Shown are the first five anodes and respective charges of the first photon in Figure 4.4. Negative values in the electron number result from the Gaussian distribution that was added when calculating the charges at the anodes. The binary results are obtained by converting the results from 4.5a via the IEEE-754 standard.

4.1.2 Reconstruction of the Initial Interaction Position and Photon Energy, Visualization of the Photon Interactions

In order to analyze the data that will be sent from the FPGA to the read-out electronics, which is representative of the data that the detector FEE will send to the read-out electronics once the mission is in orbit, a module to reconstruct the initial interaction position and photon energy that are entailed in the data was developed in Python 3.6. The reconstructed positions are then used to visualize the interactions of the photons with the detector in order to test the electronics that, once the mission is in orbit, will reconstruct the initial interaction position and photon energy.

Reconstruction of the Initial Interaction Position and Photon Energy

After reading in the files created in the previous module, the data are separated into lists such that each list contains the information for one photon[4]. That way, each photon

[4]For the binary files, the 48 bit strings are separated into 16 bit (anode positions) and 32 bit (number of electrons at anodes) strings and then converted to floating numbers using the IEE-754 standard mentioned above.

can be analyzed separately[5] by performing a fit for Equation (3.6)[6] in order to find the total number of electrons $N_{e^-,tot}$, the initial y-position y_0 and the charge cloud size σ. The photon energy is calculated by

$$E_{phot} = N_{e^-,tot} \cdot E_{average} \quad , \tag{4.5}$$

where $E_{average} = 3.6\,\text{eV}$ is the average energy needed to create an electron-hole-pair in silicon. Since the initial y-position is directly found with the curve fit, the only parameter missing is the initial x-position x_0. As mentioned in Chapter 3, the coordinate system is chosen in a way such that the anodes are located at the zero coordinate, meaning that the drift distance x_D is equal to x_0. Therefore, solving Equation (3.4) for the drift distance and substituting x_0 for x_D yields

$$x_0 = (\frac{\sigma}{6}^2 - \sigma_0^2) \cdot q \cdot \frac{E}{2k_B T} \quad , \tag{4.6}$$

with the drift field E, the Boltzmann constant k_B, the temperature T, the elementary charge q, and the initial cloud size σ_0. Since the charge cloud size was multiplied by six in order to get the full cloud width in the previous module, it has to be divided by six now to calculate the correct initial x-position. The results for the photon energy and initial interaction positions are then saved in a new file.

Visualization of the Photon Interactions with the Detector

The visualization of the initial photon interactions with the detector is made possible by a module that uses the reconstructed interaction positions to create a color map of the detector. The more a pixel of the detector interacts with photons, the redder it becomes on the color map. This can be seen in Figure 4.6, where the reconstructed interaction of a photon beam with the detector is visualized. This beam, which had a width of 100 µm, was centered at an initial interaction position of $x_0 = 10{,}000\,\mu\text{m}$ and $y_0 = 32{,}550\,\mu\text{m}$, and consisted of 50,000 photons with an energy of 4.5 keV.

4.1.3 Testing the Software Component

To test how well the initial interaction position and photon energy are reconstructed, two sets of data were produced. Since the data sent from the FEE of the FPGA to

[5] In case separate files for each photon were produced in the previously described module, an option is available to analyze these files or even only one of the files. This option works the same way as the option described here.

[6] For this fit, the baseline level due to common-mode noise K is set equal to 0 because there is no common-mode noise in the simulation.

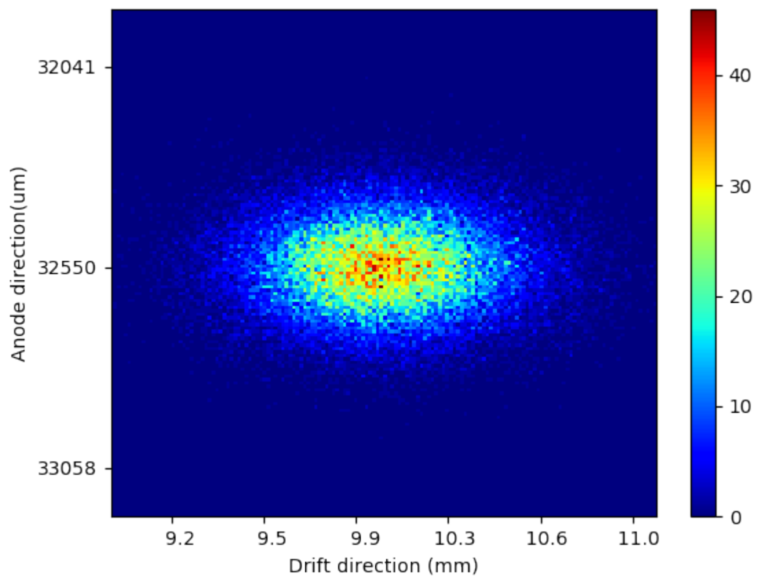

Figure 4.6: The results of visualizing the photon beam interaction with the detector. The photon beam, which had a width of 100 µm, was centered at an initial interaction position of $x_0 = 10{,}000$ µm and $y_0 = 32{,}550$ µm, and consisted of 50,000 photons with an energy of 4.5 keV. These initial values were reconstructed with the method explained in Section 4.1.2. The colorbar shows the pixel color and the respective number of reconstructed photon interactions.

the read-out electronics are in binary format, the reconstruction and analysis was done using the binary files created in the previous module.

The first dataset was used to test the reconstruction of the photon energy, and 100 photons per energy (2, 5, 10, 15, 20, 25, 30, 35, 40, 45 and 50 keV) interacted with the detector in 100 randomly selected positions as shown in Figure 4.7.

The results for the reconstructed energies are shown in Table 4.1. The average reconstructed energies across the detector were found and the standard deviation for each energy was calculated with

$$std\_dev = \sqrt{\frac{\sum_{i=0}^{N}(E_i - E_{mean})^2}{N}} \quad , \tag{4.7}$$

where $N = 10{,}000$ is the number of photon interactions for each energy, E_i are the reconstructed energies for the single photon events and E_{mean} is the average reconstructed energy. It can be seen that the standard deviation ranges from 0.11-2.26 keV. This span is due to the fitting process, where, in some cases, one of the two initial interaction positions is not reconstructed properly neither due to a domination by the value chosen for the noise simulation, in this case $\sigma = 3$ electrons. Since the standard deviation for the energies is less than 1 keV (except for 35 keV and 50 keV, where the standard deviations are 1.21 keV and 2.26 keV, respectively, due to the reasons discussed above), it can be said that the energy reconstruction from the binary data is very accurate.

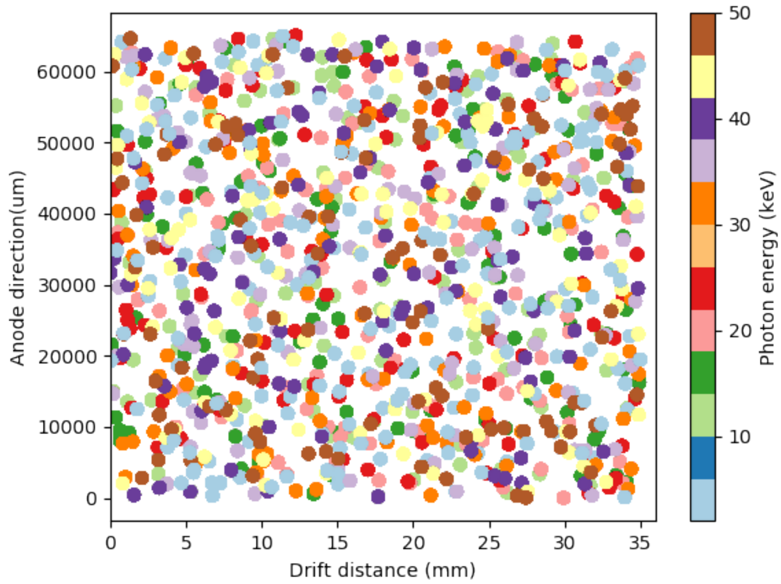

Figure 4.7: The photon interactions used for the energy reconstruction. The different colors represent the different photon energies in keV.

Table 4.1: The results of the energy reconstruction across the detector. Shown are the theoretical energy, the average reconstructed energies and the standard deviation.

Theoretical Energy (keV)	Average reconstructed energy (keV)	Standard Deviation (keV)
2	2.00	0.11
5	5.00	0.17
10	9.99	0.20
15	15.00	0.24
20	20.00	0.36
25	24.97	0.68
30	29.97	0.99
35	34.96	1.21
40	39.97	0.75
45	44.99	0.70
50	49.87	2.26

To test how well the initial interaction positions are reconstructed, a second dataset was created. In this data set, 100 positions were chosen, at which 100 photons of each energy (2, 10, 20, 30, 40 and 50 keV) interacted with the detector as shown in Figure 4.8. In addition to the interaction positions, Figure 4.8 shows the standard deviation for each position found across all energies. The standard deviations in anode direction are so small that they cannot be seen. The standard deviations in drift direction however vary, being larger for longer drift distances. A possible explanation is that for bigger initial positions in drift direction, the charge cloud upon reaching the anodes is bigger, meaning that more anodes register a smaller charge above the noise level. Since more anodes need to be fitted with Equation (3.6), the resulting variation in charge cloud sizes and therefore drift distances due to the fitting process is bigger than for smaller incident positions in drift direction. Overall, the standard deviation in drift direction varies from 0.0015-2.048 mm, while the one in anode direction is in the range of 0.537-69.717 µm. Therefore, as mentioned in Section 3.2, the reconstruction in anode direction is much more accurate than in drift direction due to the fitting process explained in Chapter 3.

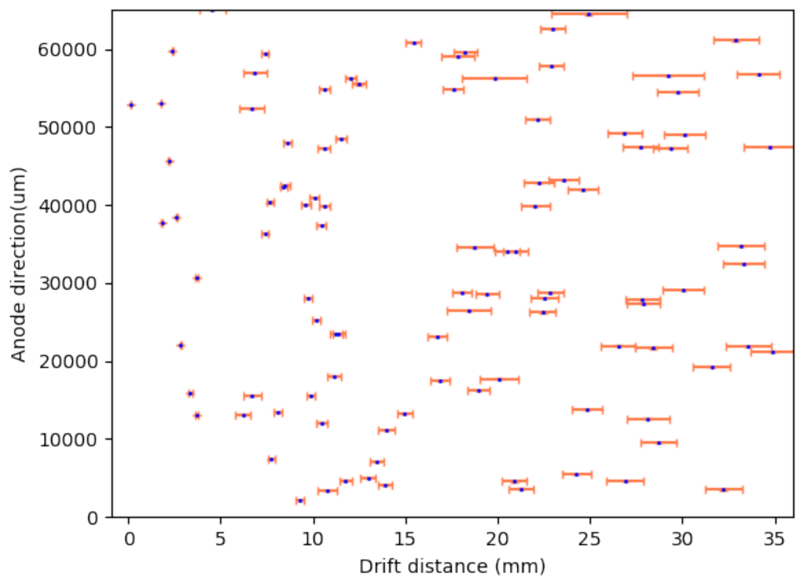

Figure 4.8: Results of the incident interaction position reconstruction. Shown are the initial interaction positions and their respective standard deviations. The standard deviation in drift direction varies from 0.0015-2.048 mm, while the one in anode direction is in the range of 0.537-69.717 µm and can therefore not be seen.

4.1.4 Communication with the FPGA

In order to properly simulate the detector and its FEE, the binary data file that was created in the software component of the detector simulator has to be sent to the hardware component, consisting of an FPGA. From here, the data will be sent out as described in Section 4.2.3. The data are sent to the FPGA bit-wise via a USB cable by executing the respective Python script in the command prompt.

Once all data are stored on the FPGA, a second script that will send a "send data" command to the FPGA can be executed. These "send data" commands are generated and sent in random intervals to provide a realistic simulation of the detector, which does not interact with photons in regular intervals. Depending on the amount of photon interactions stored on the FPGA, the maximum number of "send data" commands that should reach the FPGA can be set.

4.2 The Hardware Component of the Simulator

The hardware component of the simulator was programmed in VHDL[7] and then configured into an FPGA, which is described in Section 4.2.1. It has two tasks. The first one is to store the anode position and the number of electrons at each anode for multiple photons in a RAM. The second task is to send the data to the connected electronics, for example read-out electronics or an oscilloscope, when the "send data" command is received. Corresponding to the data that was produced in the software component of the simulator and is now stored in the FPGA, only one half of the electrically divided detector is simulated.

4.2.1 The FPGA

The FPGA used in the detector simulator is an *IGLOO2* FPGA from Microsemi located on the IGLOO2 evaluation kit (Figure 4.9). Just like other FPGAs, it is a kind of ASIC[8] that can be programmed by the user after its production. The memory of the *IGLOO2* can be wiped and reprogrammed electronically[9]. Although they cannot reach the functionality of dedicated ASICS, FPGAs are very suitable for hardware

[7] Very High Speed Integrated Circuit Hardware Description Language. Information about the language can for example be found in Reichhardt and Schwarz (2009).

[8] ASICs are integrated circuits that are designed for a specific purpose. More information on ASICs can be found in Smith (1997).

[9] Other kinds of FPGAs can only be programmed once or parts can be wiped by UV-light and be reprogrammed, giving the user the chance to program the FPGA in a range of one to thousands of times.

development and tests due to their cheaper production cost, shorter development times and the complex structures that can be configured into them. Another advantage of FPGAs is that the program can be changed during its usage in order to optimize it for the current task, enabling an optimal performance.

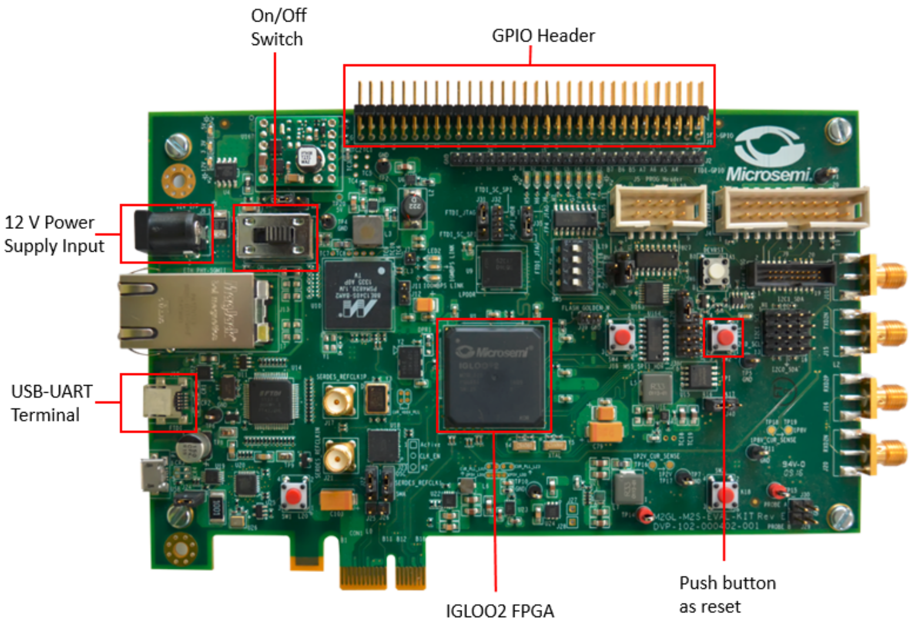

Figure 4.9: The IGLOO2 evaluation kit from Microsemi. The FPGA can be seen in the middle of the board. In addition to the FPGA, important features of the evaluation kit that will be used for the detector simulator are: the On/Off switch, the 12 V Power Supply Input, the USB-UART Terminal, the GPIO Header, and one button as reset switch. Source: Microsemi (2018).

After the *IGLOO2* is programmed and it is ensured that everything works properly, the *IGLOO2* evaluation kit is encased in an aluminum box as shown in Figure 4.10. In order to use the detector simulator, the user will have to connect the electronics to the appropriate outlets and turn on the FPGA with the "On/Off" switch located outside the box. The data are loaded from the PC onto the RAM via the USB-UART Terminal, and sent to the connected electronics via the DB-9 outlet, which is connected to the GPIO[10] Header via cables. To wipe the RAM, the reset button, connected to one of the buttons on the board, can be pushed. The connections inside the box can be seen in Figure 4.11.

4.2.2 Storing Data in the RAM

To give a realistic representation of the photon interactions with the detector, the data created in the software component of the detector simulator is stored in a RAM on the

[10]General Purpose Input/Output

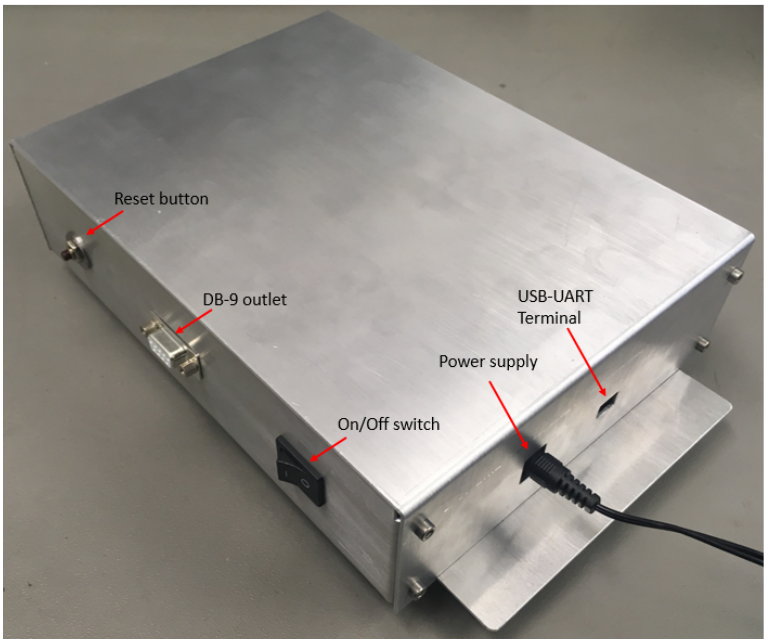

Figure 4.10: The aluminum box the IGLOO2 evaluation kit is encased in.

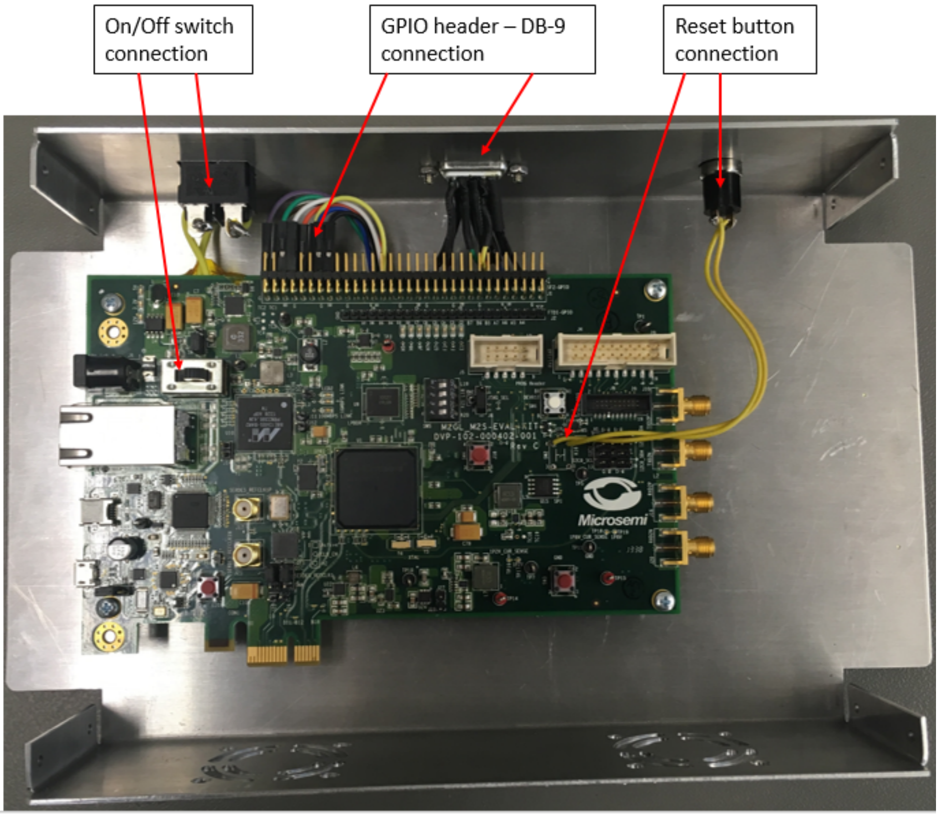

Figure 4.11: Inside view of the aluminum box the IGLOO2 evaluation kit is encased in. In order to store and retrieve the data as well as to wipe the RAM, the appropriate evaluation kit features and their counterparts outside the box are connected.

FPGA. To enable the transmission of the data to the RAM, a Universal Asynchronous Receiver and Transmitter (UART) core was implemented.

In general, the UART core sends parallel data through a serial line as shown in Figure 4.12. It is implemented because the data from the PC arrives at a different rate than the one the RAM can save the information at. The rate at which the incoming data is sampled and shifted to the respective registers is generated by the baud rate generator. One of the shift registers is the receiver, which shifts in the data sent from the PC bit-by-bit and then reassembles it. The receiver provides a mechanism to signal the availability of a new word[11] and prevents that an already received word is retrieved multiple times. As a buffer space between the receiver and the application, a receiver FiFo[12] is added. When a word is received and reassembled by the receiver, it is written to the receiver FiFo, from where the application obtains the data via the FiFo's read port at its own pace. Data that are sent from the application is stored in a transmitter FiFo. From here, the second register that is driven by the baud rate generator, the transmitter, obtains the data and loads it in parallel. These data are then shifted out and transmitted to the PC bit-by-bit at the baud rate generator's rate.

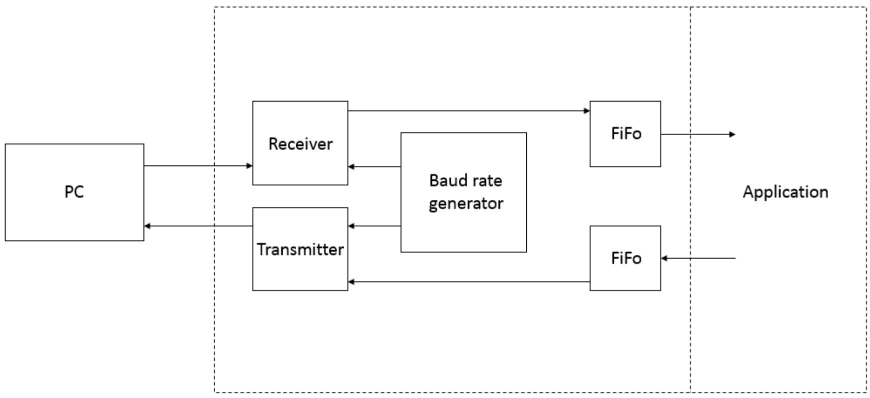

Figure 4.12: The Universal Asynchronous Receiver and Transmitter. The receiver and transmitter are driven by the baud rate generator. Once a word is received by the receiver, it is written to the FiFo (First in, First out) buffer, from where the application obtains the data. The transmitter reads the FiFo buffer which entails data from the application, and shifts the data out bit-by-bit.

[11] In this context, a word describes a data byte consisting of eight bits.

[12] *First in, First out* buffer. It is a storage between two sub-systems and is controlled by write and read operators. In the write operation, the input is written to the buffer. In the read operation, the first item in the FiFo is removed and the next item becomes available. The first item that is written to the FiFo is the one that is read out first.

In this project, the application is the RAM. A graphic representation of the RAM used in this thesis is shown in Figure 4.13. The width of the RAM is 48 bits, which is the length of each binary string containing the anode position and number of electrons at that anode. The depth of the RAM, which is represented by addresses, depends on the number of individual photon interactions $N_{interactions}$ that should be simulated and can be calculated with

$$\text{depth}_{\text{RAM}} = N_{interactions} \cdot N_{anodes} \quad . \tag{4.8}$$

Since the depth of the RAM for an Igloo2 FPGA is limited to 4096 addresses, the eXTP WFM has 448 anodes, and the number of photon interactions has to be an integer, a maximum number of nine individual photon interactions can be simulated without having to reload the RAM, leading to 4032 addresses as depth of the RAM. Each incoming data string is assigned its address and then saved in the respective slot within the RAM.

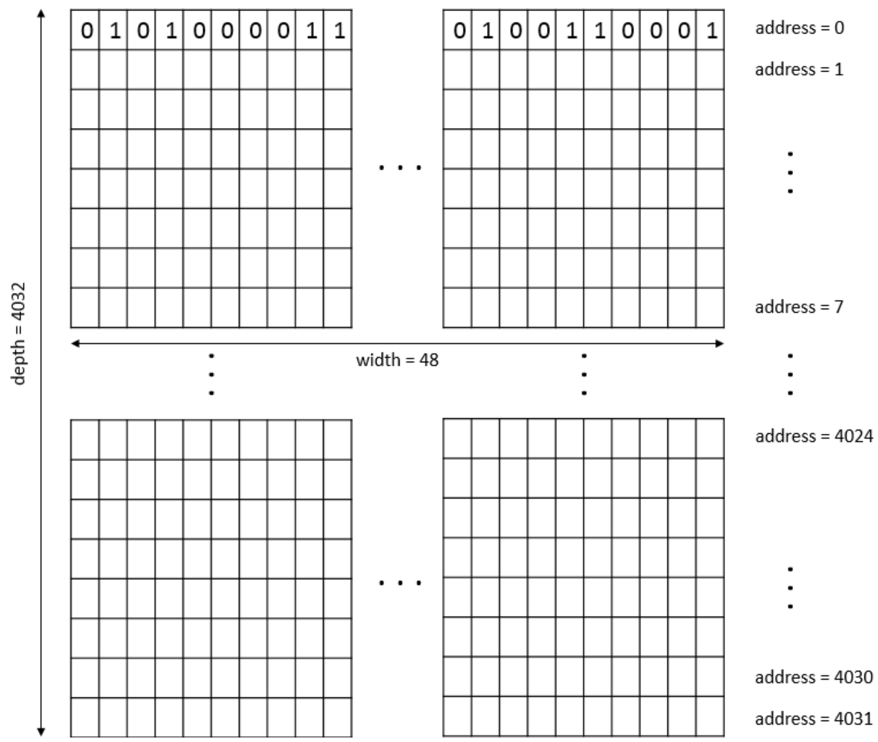

Figure 4.13: The Random Access Memory used in this thesis. The width of the RAM is 48 bits as this is the length of the binary strings received from the software component of the simulator. Since a maximum number of nine individual photon interactions can be simulated by the simulator and each interaction needs 448 addresses to store the data, the depth of the RAM is 4032 addresses.

4.2.3 Sending the Data to the Connected Electronics

Once the eXTP mission is in orbit and a photon has interacted with the detector, its FEE sends out a trigger signal to the read-out electronics. The read-out electronics answers this trigger signal with a command to send the respective data. In order to simulate this behaviour, a Serial Peripheral Interface (SPI), consisting of a master (the read-out electronics) and a slave (the FEE), was implemented to retrieve the data from the RAM.

As mentioned in Section 4.1.4, a "send data" signal is sent to the SPI master in the FPGA in order to simulate the trigger signal sent when a photon interaction took place. Once this signal is received, the master sends a trigger signal to the slave, which reads the first 448 addresses of the RAM and transmits them to the master, from where the data can be read out. By only allowing the slave to read 448 addresses at a time, single photon event simulations are enabled. Images depicting this process can be found in Section 4.2.4.

Once another "send data" signal is received by the master, meaning that a second photon interacted with the detector, and the trigger signal is sent to the slave, the next 448 addresses will be read and passed on. This can be repeated until the desired interaction number is reached. If all interactions stored on the RAM were transmitted and another "send data" signal is received by the master, the read-out process will continue with the first 448 addresses.

In future stages of this project, the master will not be programmed onto the FPGA that simulates the detector FEE, but rather be implemented in the read-out electronics that will be tested. A schematic of the final data flow achieved in this thesis is depicted in Figure 4.14.

4.2.4 Testing the Hardware Component

To test the functionality of the hardware component, mock data as shown in Figure 4.15 was sent to the RAM. The data contained 4032 lines of data, representing the anodes and the respective number of electrons for nine individual photon interactions. To check that the RAM received and stored the data correctly, the RAM addresses before and after the data was sent were compared. This comparison is depicted in Figure 4.16.

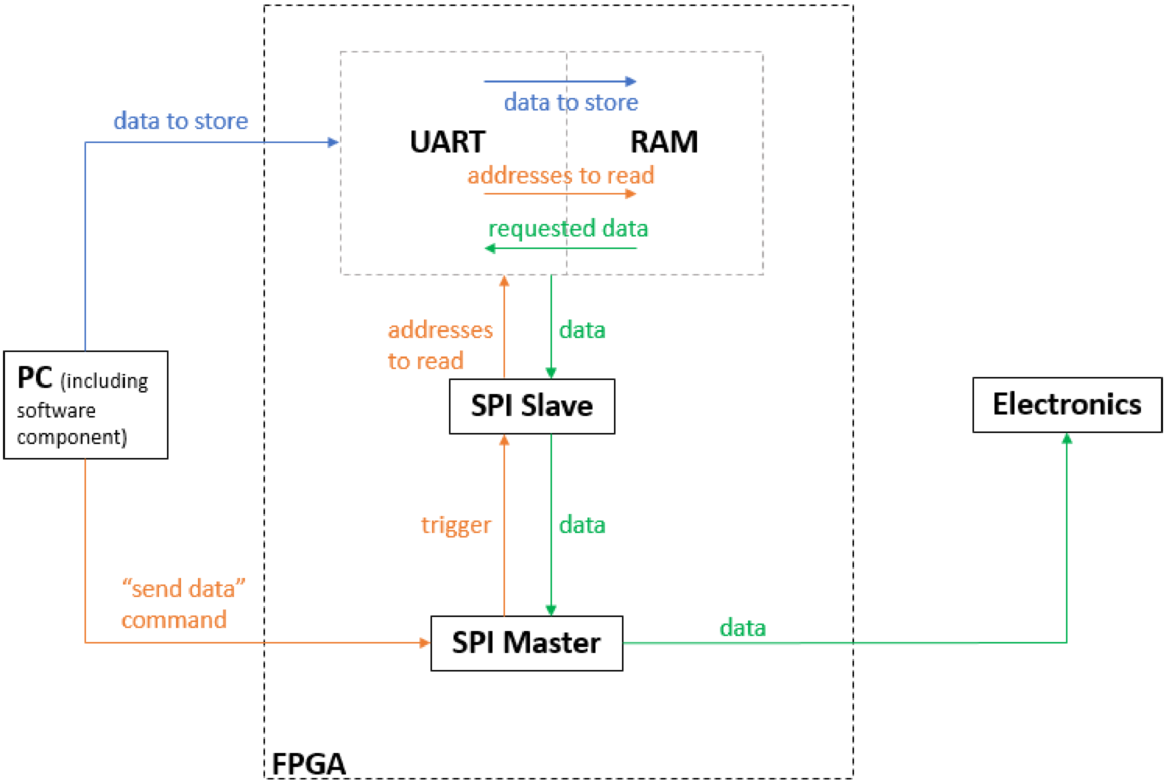

Figure 4.14: The final data flow of the detector simulator. The three components are the PC, the FPGA and the electronics that are connected to the FPGA via the DB-9 connector. The PC sends the data that was produced in the software component of the detector to the UART core, which sends it on to the RAM for storage. When the PC sends the "send data" command to the SPI master, a trigger is sent to the SPI slave to initiate reading from the RAM. The slave sends an address request consisting of 448 addresses to the UART core, which reads the data stored at the respective addresses from the RAM and sends it to the slave, from where the data flows through the master to the connected electronics.

After the data were sucessfully saved to the RAM, the FPGA was connected to an oscilloscope to check whether the data are reproduced in the correct order. The read-out process for one photon is depicted in Figure 4.17. To start the process, the "send data" command in the form of an "s" (73 in hexadecimal ASCII code) was sent to the FPGA. This notifies the SPI master to lower the "chip select" (CS) signal, which is the trigger for the SPI slave. While the master sends only zeros (MOSI, master out slave in) to the slave, the slave sends the data stored in the RAM to the master (MISO, master in slave out)[13]. Once the master received the data of one photon (448 lines), it raises the "chip select" signal and waits until another "s" is received to start the process for

[13]Both the master and the slave are shift registers, meaning that when they receive one bit, they send one bit. Because the slave does not need to store any information, the master sends only zeros in order to obtain the valuable information stored in the RAM from the slave.

the next photon. Each bit is read out with the falling edge of the clock signal (CLK). Comparing the bytes in Figure 4.17b to the ones in Figure 4.15, it can be seen that the data is read out correctly. Therefore, it can be said that the hardware component of the detector simulator is working correctly.

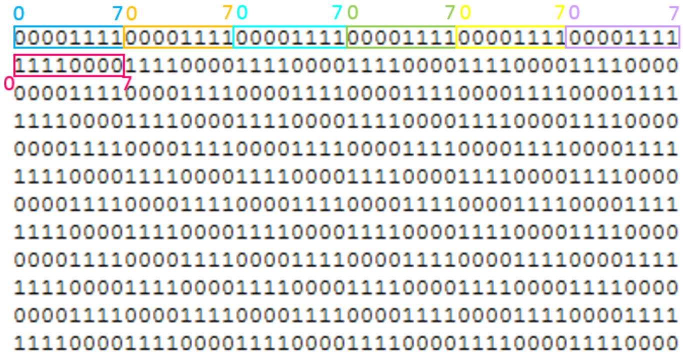

Figure 4.15: The first twelve lines of mock data sent to the FPGA's RAM. In order to see whether everything works correctly, the data were chosen to be alternating between four zeros and four ones. The colored boxes show the bytes that are pictured in 4.17b, while the numbers show the respective bit numbers of the bytes.

	0	1	2	3	4	5	6	7
0000	6E867CD3E7E8	011156360399	D48B85822611	52C5C4AC0958	9502D348ACA4	5465CE0D16B5	81D901188DE2	D90915144905
0010	EC0E3858F313	DD410D77530B	C93162431480	64550AC54D49	912C4CE84421	C7EC2484604D	386B32887F91	5B3F4A958824
0020	8DEFC341604C	09B4A81C095D	1D1D140132EA	D060B1F73411	133F90855081	671010CB5812	6C2C8B8D2E27	18A550194123
0030	5484B2812369	9F638A3411A5	4B461AC60D84	36892FB959DA	E128262A1809	10338E0DA499	A75AB2D1AC9	108541642540
0040	D0C69B04B6AD	EE0B497E0233	005259D1258B	7EE5698BF57A	A171C6B90246	620939C9430D	0F9E0E720BE0	F95664170C84

	8	9	A	B	C	D	E	F
0000	F3D60E7417E8	954821242908	3DD794C20F0	66120571F7F2	3014EEC3C0BA	E15D3F4F45D5	8F6200193325	7881CC31354A
0010	50558B30916A	CDF7AB064D0	078812C20678	382BFFDAE84D	113D5F50CF64	4F5B47095022	95C12928BCE0	D08331377488
0020	B304EC11934E	C748FEB61489	615403C214AE	C2EAB4C9ACA	80BA73441926	40884B4DF4E3	2E87B483F657	58A1910770C0
0030	40C240D3AECE	A0A8B916861F	E3A1206607A8	736757C9D5A	D5289180706D	E527182DD314	2182B168AB81	DC51913517C8
0040	76648651FB39	0A8BA94F9079	492508A60615	08420DFE5BB1	39A094893091	C196C44790C4	1CC0C9E9CDB	4A8A7325552D

(a) The RAM before sending the data.

	0	1	2	3	4	5	6	7
0000	0F0F0F0F0F0F	F0F0F0F0F0F0	0F0F0F0F0F0F	F0F0F0F0F0F0	0F0F0F0F0F0F	F0F0F0F0F0F0	0F0F0F0F0F0F	F0F0F0F0F0F0
0010	0F0F0F0F0F0F	F0F0F0F0F0F0	0F0F0F0F0F0F	F0F0F0F0F0F0	0F0F0F0F0F0F	F0F0F0F0F0F0	0F0F0F0F0F0F	F0F0F0F0F0F0
0020	0F0F0F0F0F0F	F0F0F0F0F0F0	0F0F0F0F0F0F	F0F0F0F0F0F0	0F0F0F0F0F0F	F0F0F0F0F0F0	0F0F0F0F0F0F	F0F0F0F0F0F0
0030	0F0F0F0F0F0F	F0F0F0F0F0F0	0F0F0F0F0F0F	F0F0F0F0F0F0	0F0F0F0F0F0F	F0F0F0F0F0F0	0F0F0F0F0F0F	F0F0F0F0F0F0
0040	0F0F0F0F0F0F	F0F0F0F0F0F0	0F0F0F0F0F0F	F0F0F0F0F0F0	0F0F0F0F0F0F	F0F0F0F0F0F0	0F0F0F0F0F0F	F0F0F0F0F0F0

	8	9	A	B	C	D	E	F
0000	0F0F0F0F0F0F	F0F0F0F0F0F0	0F0F0F0F0F0F	F0F0F0F0F0F0	0F0F0F0F0F0F	F0F0F0F0F0F0	0F0F0F0F0F0F	F0F0F0F0F0F0
0010	0F0F0F0F0F0F	F0F0F0F0F0F0	0F0F0F0F0F0F	F0F0F0F0F0F0	0F0F0F0F0F0F	F0F0F0F0F0F0	0F0F0F0F0F0F	F0F0F0F0F0F0
0020	0F0F0F0F0F0F	F0F0F0F0F0F0	0F0F0F0F0F0F	F0F0F0F0F0F0	0F0F0F0F0F0F	F0F0F0F0F0F0	0F0F0F0F0F0F	F0F0F0F0F0F0
0030	0F0F0F0F0F0F	F0F0F0F0F0F0	0F0F0F0F0F0F	F0F0F0F0F0F0	0F0F0F0F0F0F	F0F0F0F0F0F0	0F0F0F0F0F0F	F0F0F0F0F0F0
0040	0F0F0F0F0F0F	F0F0F0F0F0F0	0F0F0F0F0F0F	F0F0F0F0F0F0	0F0F0F0F0F0F	F0F0F0F0F0F0	0F0F0F0F0F0F	F0F0F0F0F0F0

(b) The RAM after sending the data.

Figure 4.16: Comparison of the first 80 RAM addresses before and after the data was sent. The RAM values are depicted in the hexadecimal system. As can be seen in 4.16a, the RAM is filled with random numbers before the data are received. Once the data are sent, they are correctly saved in the RAM (4.16b), which can be seen by the zero (standing for "0000") and F (standing for "1111") values.

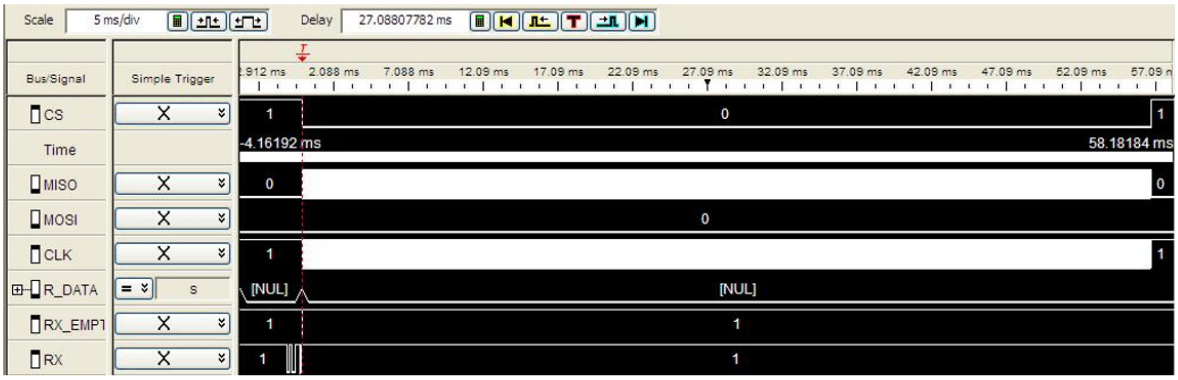

(a) The process of reading out the data for one photon.

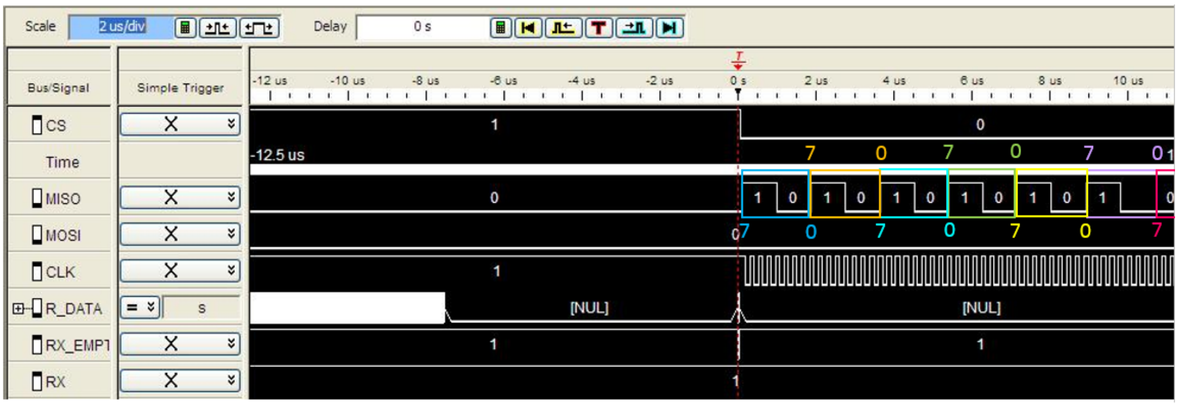

(b) Zoomed in view of the beginning of the read-out process.

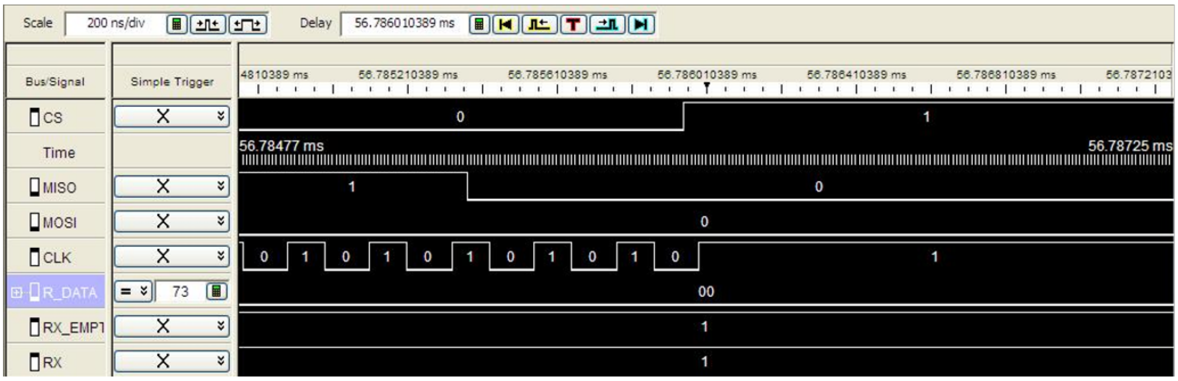

(c) Zoomed in view of the end of the read-out process.

Figure 4.17: The FPGA RAM read-out process. The process starts once the "send data" command in form of an "s" (73 in hexadecimal system) is received (R_DATA). 4.17a gives an overview over the whole process, showing that data is only received by the master (MISO, master in slave out) while the "chip select" (CS) signal is lowered, which happens once the "s" is received. 4.17b shows a zoomed in view of the beginning of the process. Each bit is read out with the falling edge of the clock signal (CLK). The colored boxes and numbers show the bytes labelled in Figure 4.15. By comparing these boxes it can be seen that the RAM is read out correctly. As 4.17c shows, the data transfer is stopped once the chip select is raised. This happens after 448 addresses are read.

5 Conclusion and Outlook

In the development stages of space missions it is important to simulate and test their components for their performance and functionality. In order to test the read-out electronics of the WFM on-board the eXTP mission, a detector simulator was developed. This simulator mimics the behaviour of the WFM's SDD and sends the respective information containing the anode position and the number of electrons at the anodes to the connected electronics.

The final version of the detector simulator is shown in Figure 5.1. The FPGA in the box communicates with the PC via the USB port, and sends the data to the oscilloscope via the DB-9 connector. With this setup, the functionality of the detector simulator can be tested. Data are sent to the FPGA via the USB cable, and once the "send data" signal is received, the data are sent to the oscilloscope to check whether they are sent in the correct order and with the correct values.

In addition to the simulator, a Python script that calculates the initial interaction position and initial photon energy from the data sent by the simulator was written. This script can be used in order to check the correct functioning of the tested read-out electronics. As shown in Section 4.1.2, the energy is reconstructed with a standard deviation of 0.1060-2.2564 keV, while the initial position is reconstructed with a standard deviation in the range of 0.0015-2.048 mm in drift direction and 0.537-69.717 µm in anode direction, respectively.

The detector simulator designed in this thesis can simulate nine individual photon interactions without having to be reloaded, and can send the information to an oscilloscope. The number of individual photon interactions that can be stored depends on the depth of the RAM, which for the Igloo2 FPGA is limited to 4096 addresses. By sending the appropriate number of "send data" commands, any amount of photon interactions can be simulated. If more than nine "send data" commands are sent before the RAM is reloaded with new data, the already stored photon information will be sent again. By reloading the RAM after the ninth photon information was sent, new

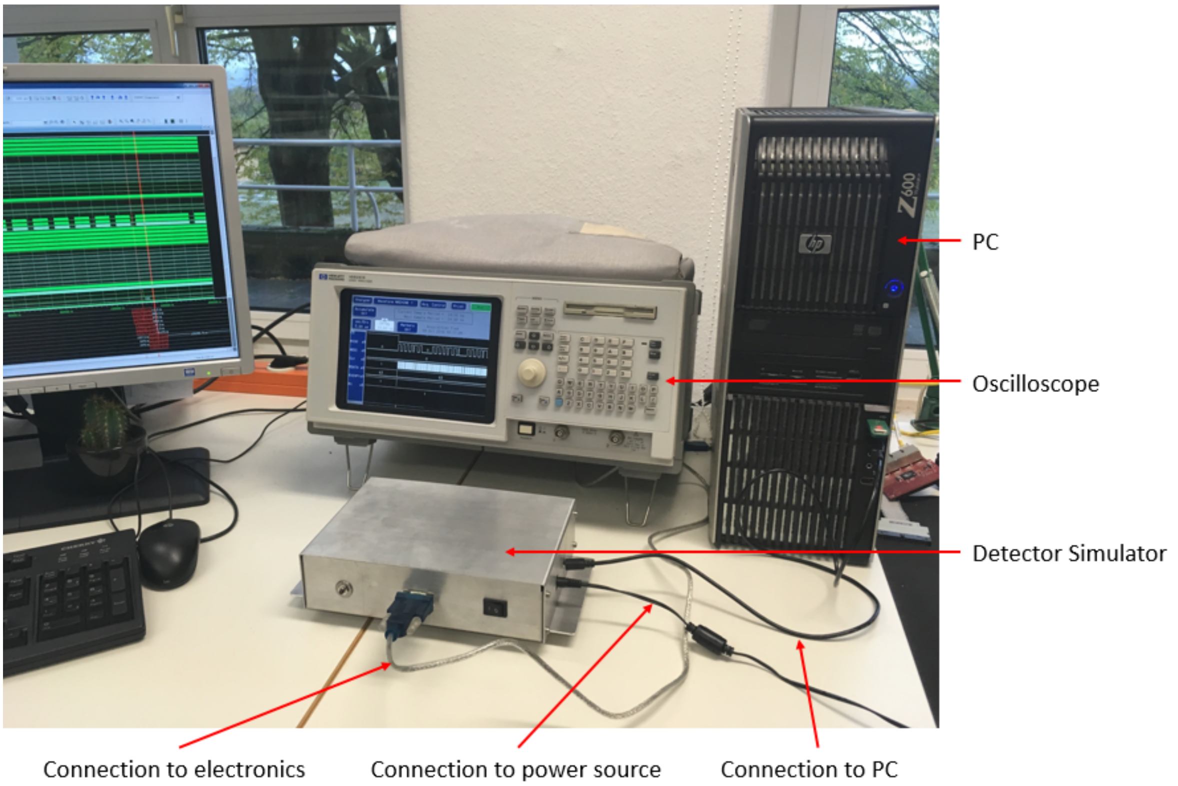

Figure 5.1: The final version of the detector simulator. The software component creating the data that is stored on the FPGA is found on the computer. Communication between the FPGA and the PC is done via the USB port, while the communication with the connected electronics is enabled by the DB-9 connection. In this setup, the connected electronics is an oscilloscope to check whether the data is sent in the correct order with the correct values.

photon information can be forwarded. However, if more than nine individual photon interactions should be simulated without having to reload data to the RAM, a different FPGA (or board) needs to be used.

Once the read-out electronics for the eXTP WFM is designed and ready to be tested, it will replace the oscilloscope that was used as the connected electronics in this thesis. For this testing, the SPI master, which currently is part of the FPGA (see Figure 4.14), will be part of the read-out electronics. With that setup, the FPGA will have to send a trigger signal to the read-out electronics to indicate a photon interaction, while the read-out electronics will be responsible to request the photon data from the simulator. future improvements of the current detector simulator should include the usage of a Rice distribution when calculating the anode noise, and the integration of a more realistic analog-to-digital conversion when converting the electron number at the anodes into binary format. Another improvement that can be made is to include the time of the photon event in the data that are transmitted to the connected electronics. Since the WFM and LAD SDD only differ in terms of anode number and anode pitch, the detector simulator is suitable to mimic the behaviour of the LAD's SDDs by adjusting these settings. Future versions of the detector simulator can include a configurability which will allow the switch between LAD and WFM detector without any adjustments. The software component of the simulator could also be adapted such that it will be able to simulate different types of detectors used in other experiments in order to test the functionality and performance of their read-out electronics. Another change that can be made to the software component is the transfer of the creation of photon interaction data to the hardware component. With this transfer, the software component would then be used solely for configuration and reconstruction purposes.

Acknowledgements

I can no other answer make but thanks, and thanks; and ever thanks.
— Shakespeare, *Twelfth Night, Or What You Will*

At the end of this thesis, there are a few people that I would like to thank:

- **Prof. Dott. Andrea Santangelo**, thank you for allowing me to write my thesis in the High-Energy Astrophysics group and for giving me a topic in the hard- and software development.
- Thank you **Dr. Chris Tenzer** for overseeing my project, for teaching me Python and VHDL, for the conversations and everything else you did. It was a great pleasure to work with you!
- **Samuel**, thank you for helping me with the hardware part of the detector. It was a lot of fun, very interesting and also entertaining to work with you.
- A huge thanks to **Eric**, **Inga** and **Sudarshan** for proofreading the thesis. Eric and Sudarshan, thank you for being great professors and even better friends that made my time in America unforgettable. You and **Christy** will forever be my American family.
- I would also like to thank the lunch group for fun conversations about any topic imaginable. A special shout out to **Inga**, **Christian** and **Sarah** for coffee breaks, serious conversations and a lot of laughter.
- Last but not least, I would like to thank my **family** and **friends** that always support me in everything I do, help me whenever they can and are always by my side. I am forever grateful that I have you in my life. I couldn't have done it without you!

List of Figures

List of Tables

List of Abbreviations

ADC Analog to digital converter

ALICE A Large Ion Collider Experiment

ASIC Application-Specific Integrated Circuit

BEE Back End Electronics

eXTP enhanced X-ray Timing and Polarimetry mission

FEE Front End Electronics

FPGA Field Programmable Gate Array

FWHM Full Width at Half Maximum

GPD Gas Pixel Detector

GRB Gamma-ray burst

IAAT Institute for Astronomy and Astrophysics Tübingen

ICU Instrument Control Unit

LAD Large Area Detector

MBEE Module Back End Electronics

MDP Minimum detectable polarization

PBEE Panel Back End Electronics

PCB Printed circuit board

PFA Polarimetry Focusing Array

QED Quantum Electrodynamics

QPO Quasi Periodic Oscillation

RAM Random-Access Memory

SDD Silicon Drift Detector

SFA Spectroscopic Focusing Array

SPI Serial Peripheral Interface

sr Steradian

UART Universal Asynchronous Receiver and Transmitter

WFM Wide Field Monitor

Bibliography

M. A. Abramowicz and O. Straub. Accretion discs. *Scholarpedia*, 9(8):2408, 2014. doi: 10.4249/scholarpedia.2408. revision #145813.

M. Alford. Color-Superconducting Quark Matter. *Annual Review of Nuclear and Particle Science*, 51:131–160, 2001. doi: 10.1146/annurev.nucl.51.101701.132449.

M. G. Alford, A. Schmitt, K. Rajagopal, and T. Schäfer. Color superconductivity in dense quark matter. *Reviews of Modern Physics*, 80:1455–1515, October 2008. doi: 10.1103/RevModPhys.80.1455.

P. A. Becker, D. Klochkov, G. Schönherr, O. Nishimura, et al. Spectral formation in accreting X-ray pulsars: bimodal variation of the cyclotron energy with luminosity. *Astronomy & Astrophysics*, 544:A123, August 2012. doi: 10.1051/0004-6361/201219065.

R. Bellazzini, L. Baldini, A. Brez, E. Costa, L. Latronico, N. Omodei, P. Soffitta, and G. Spandre. A photoelectric polarimeter based on a Micropattern Gas Detector for X-ray astronomy. *Nuclear Instruments and Methods in Physics Research Section A: Accelerators, Spectrometers, Detectors and Associated Equipment*, 510(1):176 – 184, 2003. ISSN 0168-9002. doi: https://doi.org/10.1016/S0168-9002(03)01695-4. Proceedings of the 2nd International Symposium on Applications of Particle Detectors in Medicine, Biology and Astrophysics.

R. Bellazzini, A. Brez, E.Costa, M. Minuti, et al. Photoelectric X-ray Polarimetry with Gas Pixel Detectors. *Nuclear Instruments and Methods in Physics Research Section A: Accelerators, Spectrometers, Detectors and Associated Equipment*, 720:173 – 177, 2013. ISSN 0168-9002. doi: https://doi.org/10.1016/j.nima.2012.12.006. Selected papers from the 2nd International Conference Frontiers in Diagnostic Technologies (ICFDT2).

Boella, G., Butler, R. C., Perola, G. C., Piro, L., Scarsi, L., and Bleeker, J. A. M. BeppoSAX, the wide band mission for X-ray astronomy. *Astron. Astrophys. Suppl. Ser.*, 1997. doi: 10.1051/aas:1997136.

S. Brandt, M. Hernanz, L. Alvarez, A. Argan, B. Artigues, P. Azzarello, D. Barret, C. Bozzo, E Tenzer, A. Santangelo, et al. The design of the wide field monitor for the LOFT mission. In *Space Telescopes and Instrumentation 2014: Ultraviolet to Gamma Ray*, volume 9144 of *procspie*, page 91442V, July 2014. doi: 10.1117/12.2055885.

D. N. Burrows, J. E. Hill, J. A. Nousek, J. A. Kennea, A. Wells, et al. The Swift X-Ray Telescope. *Space Science Reviews*, 120:165–195, October 2005. doi: 10.1007/s11214-005-5097-2.

R. Campana, G. Zampa, M. Feroci, A. Vacchi, et al. Imaging performance of a large-area Silicon Drift Detector for X-ray astronomy. *Nuclear Instruments and Methods in Physics Research Section A: Accelerators, Spectrometers, Detectors and Associated Equipment*, 633(1):22 – 30, 2011. ISSN 0168-9002. doi: https://doi.org/10.1016/j.nima.2010.12.237.

B. De Marco and G. Ponti. The Reverberation Lag in the Low-mass X-ray Binary H1743-322. *The Astrophysical Journal*, 826:70, July 2016. doi: 10.3847/0004-637X/826/1/70.

Y. Dong. The x-ray timing and polarization satellite - 1, 2, 3: uncovering the mysteries of black holes and extreme physics in the universe. In *Space Telescopes and Instrumentation 2014: Ultraviolet to Gamma Ray*, volume 9144 of *procspie*, page 91443O, July 2014. doi: 10.1117/12.2055333.

M. Feroci, L. Stella, M. van der Klis, T. J.-L. Courvoisier, M. Hernanz, R. Hudec, A. Santangelo, D. Walton, et al. The Large Observatory for X-ray Timing (LOFT). *Experimental Astronomy*, 34:415–444, October 2012. doi: 10.1007/s10686-011-9237-2.

M. Feroci, M. Ahangarianabhari, G. Ambrosi, F. Ambrosino, et al. The Large Area Detector onboard the eXTP mission. *Proceedings of SPIE*, 10699:10699 – 10699 – 15, 2018. doi: 10.1117/12.2312466.

Z. F. Gao, X.-D. Li, N. Wang, J. P. Yuan, et al. Constraining the braking indices of magnetars. *Monthly Notices of the Royal Astronomical Society*, 456:55–65, February 2016. doi: 10.1093/mnras/stv2465.

E. Gatti and P. Rehak. Semiconductor drift chamber — An application of a novel charge transport scheme. *Nuclear Instruments and Methods in Physics Research*, 225:608–614, 09 1984.

M. Grundmann. *The Physics of Semiconductors*. Graduate Texts in Physics. Springer International Publishing, 3 edition, 2016. ISBN 9783319238791.

M. Hernanz, S. Brandt, M. Feroci, P. Orleansky, A. Santangelo, C. Tenzer, et al. The wide field monitor onboard the eXTP mission. *Proceedings of SPIE*, 10699:10699 – 10699 – 16, 2018. doi: 10.1117/12.2313214.

IEEE. IEEE Standard for Floating-Point Arithmetic. *IEEE Std 754-2008*, pages 1–70, Aug 2008. doi: 10.1109/IEEESTD.2008.4610935.

G. K. Jaisawal and S. Naik. Detection of cyclotron resonance scattering feature in high-mass X-ray binary pulsar SMC X-2. *Monthly Notices of the Royal Astronomical Society*, 461:L97–L101, September 2016. doi: 10.1093/mnrasl/slw108.

P. Kaaret. X-Ray Polarimetry. *The WSPC Handbook of Astronomical Instrumentation*, August 2014.

E. M. Kellogg. X-Ray Observations of the Crab Nebula. In R. D. Davies and F. Graham-Smith, editors, *The Crab Nebula*, volume 46 of *IAU Symposium*, page 42, 1971.

D. Klochkov, V. Doroshenko, A. Santangelo, R. Staubert, G. Pühlhofer, et al. Outburst of GX 304-1 monitored with INTEGRAL: positive correlation between the cyclotron line energy and flux. *Astronomy & Astrophysics*, 542:L28, June 2012. doi: 10.1051/0004-6361/201219385.

H. A. Krimm, S. T. Holland, R. H. D. Corbet, A. B. Pearlman, et al. The Swift/BAT Hard X-Ray Transient Monitor. *The Astrophysical Journal Supplement Series*, 209 (1):14, 2013.

H. Li, H. Feng, F. Muleri, R. Bellazzini, et al. Assembly and test of the gas pixel detector for X-ray polarimetry. *Nuclear Instruments and Methods in Physics Research A*, 804: 155–162, December 2015. doi: 10.1016/j.nima.2015.09.060.

U. Lombardo and H.-J. Schulze. Superfluidity in Neutron Star Matter. In D. Blaschke, N. K. Glendenning, and A. Sedrakian, editors, *Physics of Neutron Star Interiors*, volume 578 of *Lecture Notes in Physics, Berlin Springer Verlag*, page 30, 2001.

D. H. Lumb, F. A. Jansen, and N. Schartel. X-ray Multi-mirror Mission (XMM-Newton) observatory. *Optical Engineering*, 51:51 – 51 – 11, 2012. doi: 10.1117/1.OE.51.1.011009.

R. Machleidt and D. R. Entem. Chiral effective field theory and nuclear forces. *Physics Reports*, 503(1):1 – 75, 2011. ISSN 0370-1573. doi: https://doi.org/10.1016/j.physrep.2011.02.001.

D. Maier, C. Tenzer, and A. Santangelo. Point and Interval Estimation on the Degree and the Angle of Polarization: A Bayesian Approach. *Publications of the Astronomical Society of the Pacific*, 126:459, May 2014. doi: 10.1086/676820.

R. K. Manchanda, A. Bazzano, C. D. La Padula, V. F. Polcaro, and P. Ubertini. Line feature around 73 keV from the Crab Nebula. *The Astrophysical Journal*, 252: 172–178, January 1982. doi: 10.1086/159543.

W. H. McMaster. Polarization and the Stokes Parameters. *American Journal of Physics*, 22:351–362, September 1954. doi: 10.1119/1.1933744.

A. Merloni, P. Predehl, W. Becker, H. Böhringer, T. Boller, A. Sasaki M. Brunner, H. Santangelo, and t. German eROSITA Consortium. eROSITA Science Book: Mapping the Structure of the Energetic Universe. *ArXiv e-prints*, September 2012.

Microsemi. IGLOO2 Evaluation Kit, 2018.

R. P. Mignani, V. Testa, D. Gonzalez Caniulef, R. Taverna, et al. Evidence of vacuum birefringence from the polarisation of the optical emission from an Isolated Neutron Star. *ArXiv e-prints*, October 2017.

T. Mihara, M. Sugizaki, M. Matsuoka, H. Tomida, et al. MAXI: all-sky observation from the International Space Station. In *Space Telescopes and Instrumentation 2014: Ultraviolet to Gamma Ray*, volume 9144 of *procspie*, page 91441O, July 2014. doi: 10.1117/12.2055792.

F. Muleri, P. Soffitta, L. Baldini, R. Bellazzini, et al. Low energy polarization sensitivity of the Gas Pixel Detector. *Nuclear Instruments and Methods in Physics Research Section A: Accelerators, Spectrometers, Detectors and Associated Equipment*, 584(1): 149 – 159, 2008. ISSN 0168-9002. doi: https://doi.org/10.1016/j.nima.2007.09.046.

F. Muleri, P. Soffitta, L. Baldini, R. Bellazzini, et al. Spectral and polarimetric characterization of the Gas Pixel Detector filled with dimethyl ether. *Nuclear Instruments and Methods in Physics Research Section A: Accelerators, Spectrometers, Detectors and Associated Equipment*, 620(2):285 – 293, 2010. ISSN 0168-9002. doi: https://doi.org/10.1016/j.nima.2010.03.006.

A. A. Mushtukov, J. Poutanen, V. F. Suleimanov, S. S. Tsygankov, et al. On the origin of cyclotron lines in the spectra of X-ray pulsars. In *European Physical Journal Web of Conferences*, volume 64 of *European Physical Journal Web of Conferences*, page 02005, January 2014. doi: 10.1051/epjconf/20136402005.

B. N. Narozhny and A. Levchenko. Coulomb drag. *Reviews of Modern Physics*, 88(2): 025003, April 2016. doi: 10.1103/RevModPhys.88.025003.

NASA. James Webb Space Telescope, 2018.

H. Noda. *X-ray Studies of the Central Engine in Active Galactic Nuclei with Suzaku.* Springer Theses. 2015. ISBN 9789812877215.

R. Novick, J. R. P. Angel, and R. S. Wolff. *Upper Limit of the X-ray Polarization of the Crab Nebula*, pages 54–64. Springer Netherlands, Dordrecht, 1971. ISBN 978-94-010-3087-8. doi: 10.1007/978-94-010-3087-8_6.

L. Pacciani, G. Di Persio, M. Feroci, P. Soffitta, et al. The sensitivity of a photoelectric X-ray polarimeter for Astronomy: The impact of gas mixture and pressure. In *Proceedings of SPIE - The International Society for Optical Engineering*, volume 4843, 02 2003.

M. Pavlinsky, R. Sunyaev, E. Churazov, M. Gilfanov, et al. Spectrum-Roentgen-Gamma astrophysical mission - art. no. 70110H. In *Proceedings of SPIE - The International Society for Optical Engineering*, volume 7011, 08 2008.

PNDetector. *Silicon Drift Detector*, 2013.

D. Psaltis, F. Özel, and D. Chakrabarty. Prospects for Measuring Neutron-star Masses and Radii with X-Ray Pulse Profile Modeling. *The Astrophysical Journal*, 787:136, June 2014. doi: 10.1088/0004-637X/787/2/136.

B. D. Ramsey. Replicated Nickel Optics for the Hard-X-Ray Region. *Experimental Astronomy*, 20(1):85–92, Dec 2005. ISSN 1572-9508. doi: 10.1007/s10686-006-9033-6.

J. Reichhardt and B. Schwarz. *VHDL-Synthese*. Oldenbourg Wissenschaftsverlag GmbH, 2009. ISBN 9783486589870.

C. S. Reynolds. Compton Reflection and Iron Fluorescence in Active Galactic Nuclei and Galactic Black Hole Candidates. In J. Poutanen and R. Svensson, editors, *High Energy Processes in Accreting Black Holes*, volume 161 of *Astronomical Society of the Pacific Conference Series*, page 178, 1999.

S. O. Rice. Mathematical Analysis of Random Noise. *Bell System Technical Journal*, 24(1):46–156, 1945. doi: 10.1002/j.1538-7305.1945.tb00453.x.

Sacek,V. Point Spread Function (PSF), 2015.

A. Sagdeo, S. K. Rai, G. S. Lodha, K. P. Singh, et al. X-ray characterization of thin foil gold mirrors of a soft X-ray telescope for ASTROSAT. Characterization of SXT mirrors by X-ray reflectivity. *Experimental Astronomy*, 28:11–23, August 2010. doi: 10.1007/s10686-010-9183-4.

K. P. Singh. Grazing incidence optics for X-ray astronomy: X-ray optics. *Journal of Optics*, 40, 09 2011.

M.J.S. Smith. *Application Specific Integrated Circuits*. Addison-Wesley VLSI systems series. Addison-Wesley, 1997. ISBN 9780201500226.

Snowden, S. L. South Atlantic Anomaly, 2002.

P. Soffitta, X. Barcons, R. Bellazzini, et al. XIPE: the X-ray imaging polarimetry explorer. *Experimental Astronomy*, 36(3):523–567, Dec 2013. ISSN 1572-9508. doi: 10.1007/s10686-013-9344-3.

L. Strüder, P. Lechner, and P. Leutenegger. Silicon drift detector - the key to new experiments. *Naturwissenschaften*, 85:539–543, 1998.

J. H. Swank. The Rossi X-Ray Timing Explorer. *Nuclear Physics B Proceedings Supplements*, 69:12–19, January 1999. doi: 10.1016/S0920-5632(98)00175-3.

The ALICE Collaboration, K. Aamodt, A. Abrahantes Quintana, R. Achenbach, et al. The ALICE experiment at the CERN LHC. *Journal of Instrumentation*, 3(08): S08002, 2008.

A. L. Watts, N. Andersson, D. Chakrabarty, M. Feroci, et al. Colloquium: Measuring the neutron star equation of state using x-ray timing. *Rev. Mod. Phys.*, 88:021001, Apr 2016. doi: 10.1103/RevModPhys.88.021001.

M. Weisskopf. An Overview of X-Ray Polarimetry of Astronomical Sources. *Galaxies*, 6(1):33, Mar 2018. ISSN 2075-4434.

M. C. Weisskopf, B. Ramsey, S. O'Dell, A. Tennant, et al. The Imaging X-ray Polarimetry Explorer (IXPE). In *Space Telescopes and Instrumentation 2016: Ultraviolet to Gamma Ray*, volume 9905 of *procspie*, page 990517, July 2016. doi: 10.1117/12.2235240.

Wikipedia contributors. Polarization (waves) — Wikipedia, the free encyclopedia, 2018.

R. S. Wolff, J. R. P. Angel, R. Novick, and P. vanden Bout. Search for Polarization in the X-Ray Emission of the Crab Nebula. *The Astrophysical Journal*, 160:L21, April 1970. doi: 10.1086/180515.

Woodruff, J. *Lexikon der Astronomie*. 1 edition, 2007.

S. N. Zhang, M. Feroci, A. Santangelo, Y. W. Dong, et al. eXTP: Enhanced X-ray Timing and Polarization mission. In *Space Telescopes and Instrumentation 2016: Ultraviolet to Gamma Ray*, volume 9905 of *procspie*, page 99051Q, July 2016. doi: 10.1117/12.2232034.

S. N. Zhang, A. Santangelo, M. Feroci, Y. Xu, et al. The enhanced X-ray Timing and Polarimetry mission- eXTP. *Sci. China-Phys. Mech. Astron.*, 60, 2018.